INTERNATIONAL JOURNAL FOR NUMERICAL AND ANALYTICAL METHODS IN GEOMECHANICS
Int. J. Numer. Anal. Meth. Geomech. 2008; **32**:915–948
Published online 17 August 2007 in Wiley InterScience (www.interscience.wiley.com). DOI: 10.1002/nag.651

SANISAND: Simple anisotropic sand plasticity model

Mahdi Taiebat[1,‡] and Yannis F. Dafalias[1,2,*,†]

[1]*Department of Civil and Environmental Engineering, University of California, Davis, CA 95616, U.S.A.*
[2]*Department of Mechanics, School of Applied Mathematical and Physical Sciences, National Technical University of Athens, Zographou 15780, Greece*

SUMMARY

SANISAND is the name used for a family of simple anisotropic sand constitutive models developed over the past few years within the framework of critical state soil mechanics and bounding surface plasticity. The existing SANISAND models use a narrow open cone-type yield surface with apex at the origin obeying rotational hardening, which implies that only changes of the stress ratio can cause plastic deformations, while constant stress-ratio loading induces only elastic response. In order to circumvent this limitation, the present member of the SANISAND family introduces a modified eight-curve equation as the analytical description of a narrow but closed cone-type yield surface that obeys rotational and isotropic hardening. This modification enables the prediction of plastic strains during any type of constant stress-ratio loading, a feature lacking from the previous SANISAND models, without losing their well-established predictive capability for all other loading conditions including the cyclic. In the process the plausible assumption is made that the plastic strain rate decomposes in two parts, one due to the change of stress ratio and a second due to loading under constant stress ratio, with isotropic hardening depending on the volumetric component of the latter part only. The model formulation is presented firstly in the triaxial stress space and subsequently its multiaxial generalization is developed following systematically the steps of the triaxial one. A detailed calibration procedure for the model constants is presented, while successful simulation of both drained and undrained behavior of sands under constant and variable stress-ratio loadings at various densities and confining pressures is obtained by the model. Copyright © 2007 John Wiley & Sons, Ltd.

Received 31 March 2007; Accepted 13 June 2007

KEY WORDS: anisotropy; sand; constitutive relations; plasticity; critical state

*Correspondence to: Yannis F. Dafalias, Department of Civil and Environmental Engineering, University of California at Davis, One Shields Ave., Davis, CA 95616, U.S.A.
†E-mail: jfdafalias@ucdavis.edu
‡E-mail: mtaiebat@ucdavis.edu

Contract/grant sponsor: National Science Foundation; contract/grant number: CMS-02-01231

1. INTRODUCTION

Development and evaluation of comprehensive constitutive models that can reliably simulate the complex stress–strain behavior of sands and yet are conceptually simple and computationally efficient in an iterative process. SANISAND is the name used for a family of Simple ANIsotropic SAND constitutive models (the name resulting from the foregoing uppercase letters) developed over the past few years [1–4], within the framework of critical state soil mechanics and bounding surface plasticity. So far the SANISAND models had a narrow wedge-type open yield surface in the triaxial p–q space with apex at the origin, which implies that only changes of the stress ratio $\eta = q/p$ can cause the necessary relative shearing and rolling of sand grains that are macroscopically modeled as plastic shear and volume deformations. According to these previous versions of the model, an increase in stress under a constant stress ratio that lies within the yield surface causes only elastic strain. This was corroborated by the very small change of void ratio observed over significant changes of confining pressures under constant stress-ratio loading for sand samples which at least are not very loose, and when grain crushing does not take place. The narrowness of the wedge was necessary for simulations of reverse and cyclic loading. The present member of the SANISAND family introduces a number of modifications in order to extend the range of applicability to constant stress-ratio loading paths and, thus, address the issue of plastic strains in the cases of very loose sands and very high pressures causing grain crushing. In other works, which consider the plastic deformation under constant-η loading paths, additional mechanism such as p-controlling cap was adopted as is carried out, for example, in double hardening sand model by Vermeer [5], and in the models by Sture *et al*. [6], Yang *et al*. [7], and Wang *et al*. [8]. However, the use of a separate loading mechanism for the cap results into formidable complication of the formulation and implementation [9–11]. The more traditional approach of using closed yield surfaces intersecting the p-axis, such as in the original or modified Cam-Clay models, creates the following unacceptable paradox: one can follow a neutral loading path starting at the point of intersection of the yield surface with the p-axis and moving tangentially along the surface, thus, changing drastically the stress ratio without inducing any plastic deformation, contrary to experimental evidence for sands (if not for clays). Because sand deforms primarily under stress-ratio changes, such yield surface shapes are in general unacceptable and should be avoided.

To bypass all these complexities and yet capture the elasto-plastic response under constant-η loading, a modified eight-curve equation in the p–q space has been adopted as the analytical expression for the yield surface, which very much resembles the narrow open wedge used in the previous versions of SANISAND, except that it is a closed surface in the p direction, which can rotate during loading around the origin in order to address the reverse loading response. These features enable the prediction of plastic strains during any type of constant stress-ratio loading, including of course the isotropic compression at zero stress ratio, which was lacking from the previous SANISAND models, without losing the well-established predictive capability of SANISAND for all other loading conditions. In fact, a number of simplifications in regard to the previous versions that employed the wedge-type yield surface are also introduced, such as the abandonment of discrete memory variables (initial values of internal variables), that cause increased difficulties for implicit numerical implementation. The new yield surface evolves according to combined isotropic and rotational hardening rules, the latter simulating the evolving anisotropy and defined by a variation of bounding surface technique that also introduces the concept of attractors under constant stress-ratio loading.

DOI: 10.1002/nag

With some hint from a recent publication by Collins [12], the plastic volumetric strain rate is assumed to have two parts: the first is associated with the dilatancy response in loading that involves change of stress ratio, and can be positive or negative, while the second is induced by constant stress-ratio loading associated with an increase of p and it is positive (contractive) owing to rearrangement of grains accompanied possibly by their crushing. It is only this second contribution of the plastic volumetric strain rate that controls the size (isotropic hardening) of the thin closed yield surface, and it is believed to represent an original proposition. A similar decomposition of the plastic deviatoric strain rate in two parts is assumed, in accordance with the foregoing two loading conditions for the two parts of the volumetric plastic strain rate. The second parts of the volumetric and deviatoric plastic strain rate enable to obtain a correct K_0 value that is related to constant stress-ratio loading.

Such plastic volumetric strains induced by a constant stress-ratio loading occur in practice in the following two cases. Either the sample is very loose and deforms at moderate pressures without crushing of the grains, or for very high pressures constant stress ratio can cause volumetric and deviatoric plastic strains irrespective of density, which are usually followed by grain crushing. Either case can be simulated with the present version of SANISAND on the basis of a constitutive ingredient that is a slight modification of a proposition by Pestana and Whittle [13, 14], which introduced the concept of the limiting compression curve (LCC) in conjunction with a bounding surface technique applied to such constant stress-ratio loading, as it will be described in detail in the sequel.

The constitutive formulation is presented in detail in both triaxial and multiaxial spaces in Sections 2 and 3. The generalization from the triaxial to multiaxial space is done systematically, equation by equation, and in a way that instructs the reader to apply the approach of generalization to other cases as well. A step-by-step calibration process for the model constants is given in Section 4, and the model performance in simulating experimental data under various loading paths and drainage conditions is presented in Section 5.

2. THE SANISAND MODEL IN THE TRIAXIAL SPACE

The framework of all versions of SANISAND models is based on the concept of critical state soil mechanics [15, 16]. Li and Wang [17] have suggested the following form for the location of critical state line (CSL) in the e–p space that has a considerable range of applicability:

$$e_c = e_0 - \lambda(p_c/p_{at})^{\xi} \tag{1}$$

where e_0, λ, and ξ are constants, p_{at} is the atmospheric pressure for normalization, and e_c and p_c refer to the critical void ratio and confining pressure, respectively. The state parameter $\psi = e - e_c$, originally, defined by Been and Jefferies [18], is a measure of how far the material state e, p (void ratio, confining pressure) is from the critical state measured along the e-axis. This has been used in all members of SANISAND in order to incorporate the critical state behavior, and it will also be used in the present version.

The schematic representations of the CSL, the state parameter ψ, and the aforementioned LCC are shown in Figure 1(a) and (b). At very high-confining pressures, the CSL could be represented with different functions than Equation (1) which are not examined in this work. Pestana and Whittle [14] have shown that the CSL and LCC are approximately parallel at high-confining pressures.

DOI: 10.1002/nag

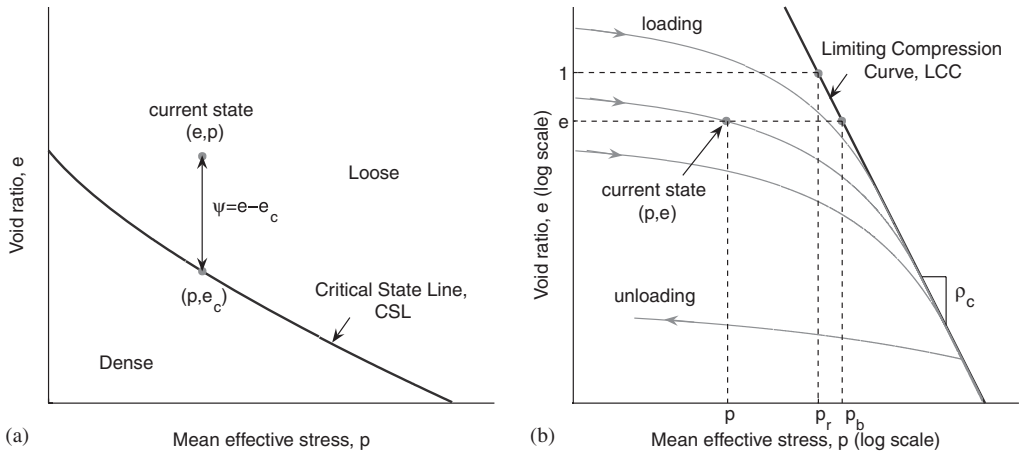

Figure 1. Schematic representations of the (a) CSL and the state parameter ψ and (b) LCC and the transitional regime concept (after Pestana and Whittle [13]).

More details on the CSL for sands including particle crushing can be found in Crouch *et al*. [19] and Russell and Kahlili [20].

The formulation of SANISAND is firstly presented in the triaxial stress–strain space in terms of the standard triaxial stress quantities $p=(\sigma_1+2\sigma_3)/3$, $q=(\sigma_1-\sigma_3)$, and strain quantities $\varepsilon_{\mathrm{v}}=(\varepsilon_1+2\varepsilon_3)$, $\varepsilon_q=2(\varepsilon_1-\varepsilon_3)/3$, where recall that $\sigma_2=\sigma_3$ and $\varepsilon_2=\varepsilon_3$. Note that in this paper all stress components are considered effective and as usual in geomechanics, both stress and strain quantities are assumed positive in compression.

Within the range of small deformations and rotations, the basic kinematical assumption of the additive decomposition of total strain rate into elastic and plastic parts is assumed, which reads

$$\dot{\boldsymbol{\varepsilon}}=\dot{\boldsymbol{\varepsilon}}^{\mathrm{e}}+\dot{\boldsymbol{\varepsilon}}^{\mathrm{p}} \tag{2}$$

where $\boldsymbol{\varepsilon}$ is a generic symbol for the strain tensor, superscripts e and p denote elastic and plastic parts, respectively, and a superposed dot denotes, henceforth, the material time derivative or the rate.

2.1. Elastic relations

For the elastic part of the model, the isotropic hypo-elasticity assumption is adopted, giving

$$\dot{\varepsilon}_q^{\mathrm{e}}=\frac{\dot{q}}{3G},\quad \dot{\varepsilon}_{\mathrm{v}}^{\mathrm{e}}=\frac{\dot{p}}{K} \tag{3}$$

where G and K are the hypo-elastic shear and bulk moduli, respectively. In a hypo-elastic description, one does not account for the existence of a potential, and G and K are the expressions of convenience. The elastic bulk modulus K is considered as a function of the confining pressure p and the current void ratio e according to

$$K=K_0 p_{\mathrm{at}}\frac{1+e}{e}\left(\frac{p}{p_{\mathrm{at}}}\right)^{2/3} \tag{4}$$

DOI: 10.1002/nag

where K_0 is a model parameter. Equation (4) is a modification of the relation used by Pestana and Whittle [13] where the exponent 1/3 was changed to 2/3 in order to get better match of available experimental results. For the elastic shear modulus G, the equation by Richards *et al*. [21] is adopted, which is again a function of p and current void ratio e as

$$G = G_0 p_{\text{at}} \frac{(2.97 - e)^2}{1 + e} \left(\frac{p}{p_{\text{at}}} \right)^{1/2} \tag{5}$$

where G_0 is a model parameter. Another possible option is to obtain K from Equation (4) and introduce a constant Poisson's ratio ν in order to calculate G from $G = 3K(1 - 2\nu)/2(1 + \nu)$.

2.2. Yield, critical, bounding and dilatancy surfaces

Earlier versions of SANISAND were assuming that plasticity occurs only when $\dot{\eta} \neq 0$. As a result, the yield surface appeared as a narrow open wedge in the p–q space with its apex at the origin, because only then when the sides of the wedge were probed, in other words only when $\dot{\eta} \neq 0$, plastic deformation took place. Since the wedge was open, radial paths inside the wedge with $\dot{\eta} = 0$ were causing only elastic strains. In order to induce plastic deformation under $\dot{\eta} = 0$ and still preserve the successful performance based on the wedge-type yield surface when $\dot{\eta} \neq 0$, one should introduce a yield surface shape that is very similar to the wedge shape, but it is also closed. Along these lines, and without the complexities of the addition of a separate closing cap (Wang *et al*. [8]) a modified version of the eight-curve equation (Lawrence [22]) is adopted for the yield surface given by

$$f = (q - p\alpha)^2 - m^2 p^2 \left[1 - \left(\frac{p}{p_0} \right)^n \right] = 0 \tag{6}$$

and plotted in Figure 2. The stress-ratio quantity α is the rotational hardening variable of the yield surface, called the back-stress ratio, and represents the slope in p–q space of the bisector of the yield surface, and p_0 represents the isotropic hardening variable and is the value of p at $\eta = \alpha$. The m is the tangent of half the opening angle of the yield surface at the origin (the total 'opening' is $2m$), and in this work, it is assumed to remain constant and very small in order to have a narrow yield surface. The narrowness of the yield surface, as for the case of the wedge type in earlier versions, is a necessary ingredient in order to address loading reversals including cyclic loading. Note that the exponent n in Equation (6) can be set to 20 as a default value. The shape of the yield surface for other values of the exponent n is shown in Figure 3 just to show the effect of this power in making a cap-like shape at the tip of the yield surface. It should be mentioned that the α, which in the multiaxial formulation will become a tensor-valued quantity, is the constitutive ingredient that renders the present version of the model anisotropic. Additional anisotropic features related to fabric can be incorporated as shown in [3, 4].

The nice property of Equation (6) is that for values of p not very close to the tip $p = p_0$ of the yield surface, the equation remains very close to a wedge-like equation in p–q space which helps to keep the well-established properties of SANISAND models in previous works that used such wedge-like yield surfaces; this is because the ratio $(p/p_0)^n$ is very close to zero when $p \ll p_0$ and n is sufficiently large. In fact by setting $p_0 \to \infty$, Equation (6) yields the equation of the wedge-type yield surface of previous versions. On the other hand, the equation creates a cap-like yield surface for values of p close enough to or at p_0 and, as a result, for constant-η stress path

DOI: 10.1002/nag

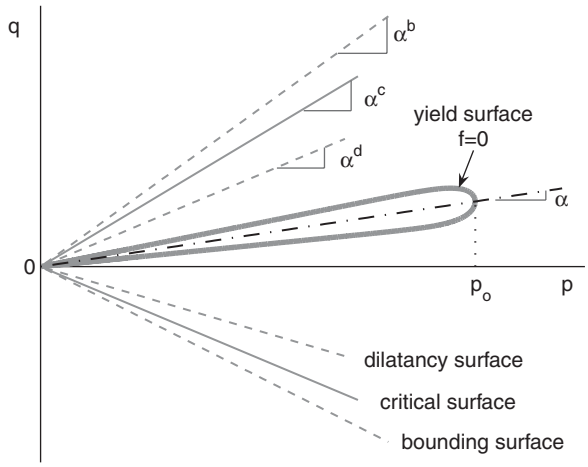

Figure 2. Schematic illustration of model surfaces in triaxial stress space.

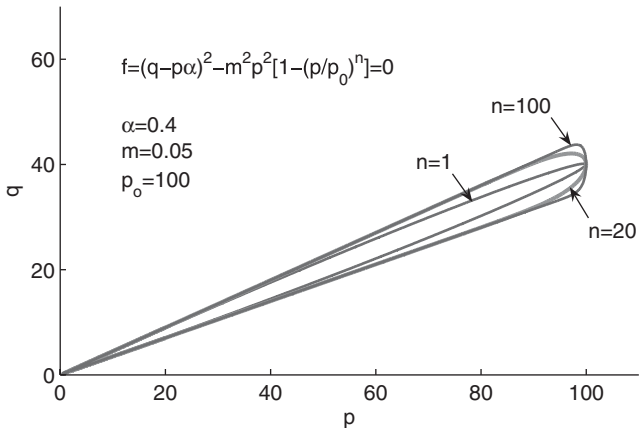

Figure 3. Illustration of the effect of power n in making a cap-like shape at the tip of the yield surface.

the closed shape of the yield surface along with an appropriate flow rule and hardening laws for p_0 and α can capture the elasto-plastic behavior.

Besides the yield surface, the model incorporates the use of three more surfaces: the critical state, bounding, and dilatancy surfaces. Traditionally these surfaces, which will appear as lines emanating from the origin in the triaxial space, are related to the stress ratio η, as, for example, when $\eta = \eta^c = M$ at critical state. Here, however, they will be associated with the back-stress ratio α based on the following rationale. From Equation (6) one can easily solve for $\eta = q/p = \alpha \pm m[1 - (p/p_0)^n]^{1/2}$. As p varies from zero to p_0, the η varies from $\eta = \alpha \pm m$ to $\eta = \alpha$, respectively. Thus, when $\eta = \eta^c = M$, it implies that accordingly the α achieves a critical value α^c that varies from

DOI: 10.1002/nag

$\alpha^c = M - m$ (for compression) at $p = 0$, to $\alpha^c = M$ at $p = p_0$. Given that m is very small (a typical default value is $m = 0.05\alpha^c$ [23]), one can assume that for all practical purposes α^c can acquire any value between $M - m$ and M. In essence we are saying that the substitution of α for η in characterizing a critical state creates no significant error due to the narrowness of the yield surface.

Thus, the three foregoing surfaces are associated with α and appear in the triaxial space as open wedges with the apex at the origin of the p–q axis. Their shapes are fully defined by slopes $\alpha_c^{c,b,d}$ for the triaxial compression and $\alpha_e^{c,b,d} = c\alpha_c^{c,b,d}$ for the triaxial extension with c the usual ratio of extension to compression quantities; the superscripts c, b, and d stand for critical, bounding, and dilatancy, respectively, while the subscripts c and e stand for compression and extension, respectively. The generic symbol $\alpha^{c,b,d}$, without a subscript c or e, can be used for either compression or extension, as shown in Figure 2. The slope α_c^c is constant related to the position of the CSL in the compression side of the p–q space (approximately $\alpha_c^c = M_c - m$), while α_c^b and α_c^d are assumed to be continuous function of the α_c^c and the everchanging value of the state parameter ψ according to [2]

$$\alpha_c^b = \alpha_c^c \exp(-n^b \psi) \tag{7}$$

$$\alpha_c^d = \alpha_c^c \exp(n^d \psi) \tag{8}$$

where n^b and n^d are the model parameters. Clearly for $\psi < 0$, $\alpha_c^d < \alpha_c^c < \alpha_c^b$, and *vice versa* for $\psi > 0$, while $\alpha_c^b = \alpha_c^d = \alpha_c^c$ at $\psi = 0$. Equations (7) and (8), proposed in [2], are of cardinal importance for the application of the model to various densities and pressures, and the implied concept of variation with ψ has been the main original contribution of the first SANISAND version [1] where a linear, instead of exponential, variation with ψ was proposed.

In a bounding surface formulation, one needs to define the 'image' of a stress-like quantity onto the bounding or similar surfaces in stress space. In triaxial space, the image of the current back-stress ratio α on the critical surface is $\alpha^c = \alpha_c^c$ when $\eta - \alpha > 0$, and it is $\alpha^c = -\alpha_e^c$ when $\eta - \alpha < 0$. In essence, the mapping from α to its images is not between points in triaxial space, but between lines with slopes α, α_c^c, and $-\alpha_e^c$. Similar mapping rule applies for the images α_c^b, $-\alpha_e^b$ and α_c^d, $-\alpha_e^d$ of α on the bounding and dilatancy surfaces, respectively. These mapping rules can be concisely expressed using the aforementioned generic symbol $\alpha^{c,b,d}$ valid for either compression or extension, in the form

$$\alpha^{c,b,d} = sg\alpha_c^{c,b,d} \tag{9}$$

where the scalar s is an auxiliary parameter taking the value of $s = +1$ for $\eta - \alpha > 0$, and $s = -1$ for $\eta - \alpha < 0$, and the scalar g is generally an interpolation function taking the value 1 for $\eta - \alpha > 0$, and c for $\eta - \alpha < 0$, with $c = \alpha_e^c / \alpha_c^c$. The general form of the interpolation function g will be defined later in the multiaxial generalization. Notice that Equation (9) can be used in conjunction with Equations (7) and (8), which in practical terms means that for $\eta - \alpha < 0$ the α_e^c must substitute for α_c^c in Equations (7) and (8).

2.3. Flow rule

Two mechanisms have been considered for the plastic strains that provide two separate contributions for each plastic strain rate triaxial component indicated by subscripts 1 and 2, and given in

DOI: 10.1002/nag

combination by

$$\dot{\varepsilon}_q^{\mathrm{p}} = (\dot{\varepsilon}_q^{\mathrm{p}})_1 + (\dot{\varepsilon}_q^{\mathrm{p}})_2 = \langle L \rangle [s r_{\mathrm{ef}} + X \eta \mathrm{e}^{-V r_{\mathrm{ef}}}] \tag{10a}$$

$$\dot{\varepsilon}_{\mathrm{v}}^{\mathrm{p}} = (\dot{\varepsilon}_{\mathrm{v}}^{\mathrm{p}})_1 + (\dot{\varepsilon}_{\mathrm{v}}^{\mathrm{p}})_2 = \langle L \rangle [D r_{\mathrm{ef}} + \mathrm{e}^{-V r_{\mathrm{ef}}}] \tag{10b}$$

$$r_{\mathrm{ef}} = |\eta - \alpha| = \left[1 - \left(\frac{p}{p_0} \right)^n \right]^{1/2} \tag{11}$$

where L is the always positive plastic loading index, otherwise known as plastic multiplier, depending on the stress rate (to be defined in the sequel). The subscript ef of r_{ef} refers to the 'effective' stress-ratio concept associated with the difference $\eta - \alpha$, and the last expression for r_{ef} in terms of p/p_0 was obtained by the virtue of Equation (6). As already mentioned in the Introduction, the motivation for decomposing the plastic strain rate in two parts came from a suggestion by Collins [12] to similarly decompose the volumetric plastic strain rate only, within a different theoretical setting.

It is important to understand at the outset the distinctive nature and mode of appearance of the first and second contributions to the plastic strain rates, expressed by the two terms in the brackets of the right-hand side of Equations (10a) and (10b). Firstly, it must be stated that V is a very large positive number; a default value $V = 1000$ is chosen in this work. Given such large value of V, the role of the quantity $\exp(-V r_{\mathrm{ef}})$ is basically that of a transition mechanism from plastic strain rates induced by loading due to stress ratio changes (the first contribution), to plastic strain rates induced by constant stress-ratio loading (second contribution) depending on the value of r_{ef}. Indeed, when the stress point in not close to the tip of the yield surface where $p = p_0$, it basically lies on the wedge-like part of the yield surface where $p/p_0 < 1$. Thus, because n is a very large number, it follows that $1 - (p/p_0)^n \simeq 1$, and as a consequence $r_{\mathrm{ef}} \simeq m$. Then, the term $\exp(-V r_{\mathrm{ef}}) \simeq 0$ because V is very large; hence, only the first contribution is practically active. But when the stress point is very close to or at the tip of the yield surface where $p \simeq p_0$, it follows that $r_{\mathrm{ef}} \simeq 0$, thus $\exp(-V r_{\mathrm{ef}}) \simeq 1$, and it is only the second contribution that is active under constant stress ratio $\eta \simeq \alpha$ loading, while the first contribution is practically zero.

Addressing now the first contribution in detail, observe that in essence it corresponds to what the previous versions of SANISAND models provided with the wedge-type open yield surfaces. The induced plastic strain rates are associated with *slipping and rolling of particles* under shear. The auxiliary parameter s takes the value 1 when $\eta - \alpha > 0$ and -1 when $\eta - \alpha < 0$, thus, one has $s r_{\mathrm{ef}} = \eta - \alpha$ always, which determines the positive or negative sign of $(\dot{\varepsilon}_q^{\mathrm{p}})_1$ in Equation (10a). All the important quantity $D = (\dot{\varepsilon}_{\mathrm{v}}^{\mathrm{p}})_1 / |(\dot{\varepsilon}_q^{\mathrm{p}})_1|$ represents the well-known dilatancy, relating deviatoric and volumetric plastic strain rates. The constitutive assumption for the dilatancy D is very simple and follows the logic of bounding surface plasticity, in that it renders D a function of the distance $\alpha^d - \alpha$. The simple linear form

$$D = s A_d (\alpha^d - \alpha) \tag{12}$$

is adopted with A_d the dilatancy parameter and α^d varying with ψ according to Equations (8) and (9). It is the sign of D that defines contraction (+) or dilation (−) depending on both the distance $\alpha^d - \alpha$ and the direction of loading *via* s. Notice the importance of ψ in determining α^d from Equations (8) and (9), and subsequently its effect on D.

DOI: 10.1002/nag

The second contribution to plastic strain rate, denoted with subscript 2 in Equations (10a) and (10b), is mainly generated under constant-η and is due to *asperities fracture and particle crushing*. X is a positive model parameter, and V is a large number, as already discussed. The reason for introducing $X\eta$ in Equation (10a) is based on the following observation. For loading $\eta = 0$ (isotropic compression), one should expect only volumetric strains for an isotropic sample, while under loading at constant $\eta \neq 0$, the presented experimental data by McDowell *et al*. [24] show that plastic deviatoric strain is created as well. The simplest way to capture both of these features is to introduce in Equation (10a) a function for the second contribution of the plastic deviatoric strain that is proportional to η such as $X\eta$. Notice that in this case one has from Equations (10a) and (10b) that $(\dot{\varepsilon}_v^p)_2/|(\dot{\varepsilon}_q^p)_2| = 1/X|\eta| \simeq \dot{\varepsilon}_v^p/|\dot{\varepsilon}_q^p|$ since the first contribution is zero when $r_{ef} = |\eta - \alpha| = 0$. Thus, the dilatancy under constant stress-ratio loading is defined by means of $1/X|\eta|$, and can be related to the K_0 value for the calibration of X.

2.4. Rate evolution equations for the internal variables

In the sequel, evolution laws for the internal variables p_0 and α are necessary. Recall that the change of α determines the rotational hardening of the model, while the change of p_0 addresses the increase in the size of the yield surface. Changes of the size of the yield surface, i.e. of p_0, are considered to be related only to the second contribution of the plastic volumetric strain rate $(\dot{\varepsilon}_v^p)_2$, given the nature of such strains. Pestana and Whittle [13] initially proposed a model for calculating such volumetric strain under isotropic consolidation, i.e. $\eta = 0$, which was later generalized to address also loading under constant stress ratio $\eta \neq 0$ [14]. The model was based on the observation that the pressure-void ratio curves of specimens compressed from different initial formation densities approach a curve at high stress levels—the LCC—which is linear in a double logarithmic void ratio-effective stress space as shown in Figure 1(b). ρ_c and p_r are the two model constants required by Pestana and Whittle proposition [13] to locate the LCC for $\eta = 0$, and their role is illustrated in Figure 1(b). The irrecoverable deformation, which represents mechanisms ranging from particle sliding and rolling at low pressures to breaking of asperities, crushing and degradation at high pressures, the principal component of the LCC regime, can be lumped together as volumetric plastic strain. Pestana and Whittle [13] have obtained the increment of the induced plastic volumetric strain using a bounding surface plasticity methodology, which requires the use of a 'distance' measure δ between the current confining pressure p and its 'image' $p_b = p_r e^{-1/\rho_c}$ on the LCC at the same void ratio, Figure 1(b). Such distance was defined by $\delta = 1 - (p/p_b)$ in [13] when isotropic consolidation at $\eta = 0$ is considered. However, under constant stress ratio loading $\eta \neq 0$ at the same confining pressure as under $\eta = 0$, data from McDowell *et al*. [24] showed that the larger the (absolute) value of η, the larger is the plastic volumetric strain rate. As a result, the pressure-void ratio curves converge with different LCC that are parallel to the LCC observed under $\eta = 0$, but displaced closer to the origin $p = 0$, such displacement being greater for larger $|\eta|$. Such relocation of the LCC can be analytically described by rendering the p_b of the expression $\delta = 1 - (p/p_b)$, a decreasing function of $|\eta|$, or equivalently of $|\alpha|$ given the closeness between $|\eta|$ and $|\alpha|$ due to the narrowness of the yield surface. The foregoing provides an interpretation of the proposition made by Pestana and Wittle [14] to generalize the definition of δ for loading under any η (or α), which with some modifications including a change of notation is expressed by the equation

$$\delta = 1 - \frac{p}{p_b}\left[1 + 2\frac{\alpha^2}{(g\alpha_c^c)^2}\right] \tag{13}$$

DOI: 10.1002/nag

Besides using α instead of η, the modifications from Reference [14] is the factor 2 added inside the bracket for better simulation of data in our case, and the presence of g to account for the difference between triaxial compression and extension, since the quantity $g\alpha_c^c$ is either α_c^c when $g=1$ for $\alpha>0$ or α_e^c when $g=c$ for $\alpha<0$; note that it is the sign of α and not that of $\eta-\alpha$ which determines the choice of the value of g, since it will be shown that at constant stress ratio loading one has $\eta-\alpha=0$. The p_b appearing in Equation (13) is associated with the LCC obtained for $\eta=0$, Figure 1(b), and the greater than one bracketed quantity in Equation (13) is a factor that can be thought that divides and reduces this p_b in order to model indirectly by such reduction the parallel translation of the LCC when $\alpha\neq 0$ as discussed earlier. Clearly when $\alpha=0$, one has $\delta=1-(p/p_b)$ as expected. Given the above definition, it is important to observe that the possibility for a negative δ can arise as follows. Assume that a loading with $\eta=\alpha=0$ takes place, and in the course of it one changes to an $\eta=\alpha\neq 0$. If the p is close enough to p_b, the greater than one value of the bracketed quantity in Equation (13) may render the δ negative, with a consequence which will be studied in the sequel.

Having defined δ, one can express the second contribution of the plastic volumetric strain rate following Pestana and Wittle [14] suggestion that, with a modification in order to account for the possibility to have $\delta<0$ and accounting for the different exponent for p/p_{at} used in Equation (4) for the elastic bulk modulus, reads

$$(\dot{\varepsilon}_{\mathrm{v}}^{\mathrm{p}})_2=\frac{e}{(1+e)}\left(\rho_c-\frac{(p/p_{\mathrm{at}})^{1/3}}{K_0}\right)(1-(\operatorname{sgn}\delta)|\delta|^{\theta})\frac{\dot{p}}{p} \tag{14}$$

where K_0 appears in Equation (4), ρ_c was already defined as the slope of the LCC in $\log e-\log p$ space, θ is a constant exponent, and $\operatorname{sgn}\delta$ means the sign of δ. The aforementioned modification from [14] consists of using the term $1-(\operatorname{sgn}\delta)|\delta|^{\theta}$ instead of $1-\delta^{\theta}$, because as already observed earlier one may have $\delta<0$ and there is a problem in raising to the θ power a negative δ. In [14], the authors simply restrict the value of δ to be positive without examining the possibility of ever becoming negative. Observe now how beneficial is such a modification that allows for a negative δ. Indeed, when $\delta<0$ the term $1-(\operatorname{sgn}\delta)|\delta|^{\theta}=1+|\delta|^{\theta}$ that implies, according to Equation (14), that an increased amount of $(\dot{\varepsilon}_{\mathrm{v}}^{\mathrm{p}})_2$ is induced for the same $\dot{p}$ compared with the case with $\delta>0$ where $1-(\operatorname{sgn}\delta)|\delta|^{\theta}=1-|\delta|^{\theta}$. Such an increase of volumetric strain will make the e–p curve converge with the relocated closer to the origin LCC from the outside, i.e. from p values larger than p_b divided by the bracketed factor of Equation (13), until asymptotically $\delta=0$ as it should. In other words, the model self-corrects a p that might be found outside its associated LCC due to a previous loading history, by sending it back to the proper LCC. This particular aspect of the model will be illustrated in Section 4.5 for calibration of the compression parameters.

Substitution of $(\dot{\varepsilon}_{\mathrm{v}}^{\mathrm{p}})_2$ from Equation (10b) and of p by p_0 in Equation (14), since for this case the stress point is at the tip of the yield surface where $p=p_0$, yields a relation when solved for $\dot{p}_0$ gives

$$\dot{p}_0=\langle L\rangle\frac{(1+e)p_0\mathrm{e}^{-Vr_{\mathrm{ef}}}}{e(\rho_c-(p_0/p_{\mathrm{at}})^{1/3}/K_0)(1-(\operatorname{sgn}\delta)|\delta|^{\theta})}=\langle L\rangle\bar{p}_0 \tag{15}$$

with the quantity $\bar{p}_0$ inferred from the equation. Thus, Pestana and Whittle's suggestion for the volumetric strain rate of the second contribution was effectively translated in terms of the isotropic hardening portrayed by $\dot{p}_0$ in Equation (15) in conjunction with the aforementioned modifications.

DOI: 10.1002/nag

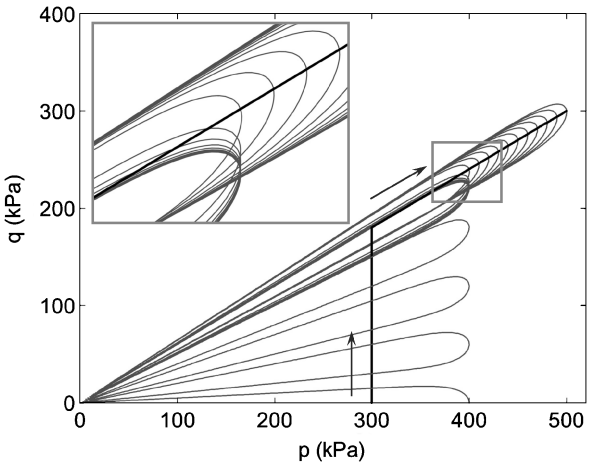

Figure 4. Illustration of the rule of attractor mechanism $|\eta - \alpha|$ in evolution of α.

For the evolution of α one is faced with two requirements. Firstly, α must converge with its bounding image α^b, which in turn varies with ψ according to Equations (7) and (9). This requirement can be fulfilled by properly introducing the term $\alpha^b - \alpha$ into the rate equation of evolution for α. Secondly, for constant-η loading the α must tend toward η, which implies that r_{ef} tends toward zero based on Equations (10a) and (10b), since this is the key to successful simulation by deactivating the first contribution while fully activating the second contribution of the plastic strains, required under constant stress-ratio loading. This is achieved by expressing the rate of α also as function of $r_{\text{ef}} = |\eta - \alpha|$, which renders η a stress-ratio 'attractor' for α, in the sense that α converges with η under constant-η loading. Thus, the foregoing two requirements can be satisfied by a simple evolution law that combines the product of both $\alpha^b - \alpha$ and $|\eta - \alpha|$, as

$$\dot{\alpha} = \langle L \rangle h |\eta - \alpha| (\alpha^b - \alpha) = \langle L \rangle h r_{\text{ef}} (\alpha^b - \alpha) = \langle L \rangle \bar{\alpha} \tag{16}$$

where the hardening modulus h is a positive function of the state in general, and the quantity $\bar{\alpha}$ is inferred from the equation for future use.

The role of the attractor term $|\eta - \alpha|$ is eloquently illustrated in Figure 4. In this figure, first a change of stress ratio from zero to a certain value induces a corresponding rotation of the yield surface as α tends toward α^b with no change in the value of p_0. Subsequently, a constant stress ratio η loading is applied. Then, on the one hand, p_0 increases, while on the other hand, the back-stress ratio α tends again toward α^b because of the term $(\alpha^b - \alpha)$ in Equation (16). However, the presence of the attractor term $|\eta - \alpha|$ in the same equation prevents α from eventually reaching α^b and, instead, forces α to tend asymptotically toward η before reaching α^b. The corresponding simulation details are shown in the insert of Figure 4.

It should be mentioned that had the loading not been constant stress-ratio type, the convergence with α^b would have prevailed over the convergence with η, along the lines of bounding surface formulation. In fact in this case, the equation for $\dot{\alpha}$ is very similar to the one postulated in the previous versions of SANISAND models with the wedge-type yield surface. Indeed recall that $r_{\text{ef}} = |\eta - \alpha| = m[1 - (p/p_0)^n]^{1/2}$, which for variable stress-ratio loading implies that $(p/p_0) < 1$, yields $|\eta - \alpha| \simeq m$; thus, the role of the attractor term $|\eta - \alpha|$ is neutralized adding simply a constant

DOI: 10.1002/nag

factor m to the equation for $\dot{\alpha}$, which can be considered part of the parameter h as in the previous versions with the open wedge yield surface type that did not need an attractor. Equation (16), with the use of the 'distance' measure $(\alpha^b - \alpha)$ and the attractor measure $|\eta - \alpha|$ multiplying each other, is based on a corresponding proposition by Dafalias *et al*. [25] in relation to the SANICLAY model for clays.

Finally, notice that because the sign of $\dot{\alpha}$ is determined from the term $\alpha^b - \alpha$, it allows for the description of softening in case $\alpha^b - \alpha < 0$ that yields $\dot{\alpha} < 0$. This can occur in the course of monotonic loading since α^b varies with ψ according to Equation (7), and consequently, it is possible for α to momentarily 'cross' a decreasing α^b in, say, triaxial compression, thus rendering $\alpha^b - \alpha < 0$, and immediately afterwards α begins to also decrease since $\dot{\alpha} < 0$ tending toward α^b. In relation to the foregoing notice that the use of the absolute value of $|\eta - \alpha|$ is necessary in order to avoid erroneous sign of $\dot{\alpha}$. One could have written, instead, $(\eta - \alpha)(\alpha_c^b - \alpha)$ for $\eta - \alpha > 0$, and $(\eta - \alpha)(\alpha_e^b + \alpha)$ for $\eta - \alpha < 0$ with exactly same results as before, recalling that Equation (9) yields $\alpha^b = \alpha_c^b$ for $\eta - \alpha > 0$ and $\alpha^b = -c\alpha_c^b = -\alpha_e^b$ for $\eta - \alpha < 0$. However, such writing would be problematic in its generalization to multiaxial stress space because of the two multiplying terms that would be tensor valued (no sense in multiplying two tensors in the present setting).

As of the value of h the simplest choice is to assume it is a constant; however, for better simulating capabilities, one can employ a nonlinear function of state variables. For this purpose Dafalias and Manzari [3] introduced an h that was a variable with e, p, and η in order to increase the efficiency of the model in capturing the nonlinear response and reverse loading. They had employed the term $|\eta - \eta_{\text{in}}|$ in the denominator of the expression for h, where η_{in} was the value of η at the initiation of a loading process. This yields an infinite h at such initiation, hence, an infinite plastic modulus and a zero loading index L, which in the current version of SANISAND prevents change of p_0 under constant-η loading; therefore, it is not appropriate for our purpose. The following form resolves the previously mentioned problem and simplifies the model implementation by removing the updatable and difficult to implicitly implement discrete memory parameter η_{in} from the model equation:

$$h = \frac{b_0}{(b_{\text{ref}} - s(\alpha^b - \alpha))^2} \tag{17a}$$

$$b_0 = G_0 h_0 (1 - c_h e) \left(\frac{p_{\text{at}}}{p} \right)^{1/2} \tag{17b}$$

h_0 and c_h are the positive model parameters, introduced in the previous version of SANISAND [3]. The important step here is the elimination of η_{in} and its substitution by a fixed reference stress-ratio distance $b_{\text{ref}} = \alpha_c^b + \alpha_e^b$, which corresponds to the 'diameter' of the bounding surface. Notice that when $s = 1$, $\alpha^b = \alpha_c^b$ and the above definition renders $b_{\text{ref}} - s(\alpha^b - \alpha) = (\alpha_e^b + \alpha)$, while for $s = -1$, $\alpha^b = -\alpha_e^b$ and $b_{\text{ref}} - s(\alpha^b - \alpha) = (\alpha_c^b - \alpha)$, recalling that α can be positive or negative. Instead of having the linear dependence of h on e, as shown in Equation (17b), one can also introduce the exponential dependence as $b_0 = G_0 h_0 \mathrm{e}^{-c_h e} (p_{\text{at}}/p)^{1/2}$. It should be mentioned that a couple of other possible choices for h function have been proposed by Manzari and Dafalias [1] and Papadimitriou *et al.* [23].

2.5. Loading index and plastic modulus

For the completion of the model, the determination of the loading index L is obtained by standard methods of plasticity [26], whereby the consistency condition $\dot{f} = 0$ is applied to Equation (6) and

DOI: 10.1002/nag

in conjunction with Equations (15) and (16) yields

$$L = \frac{1}{K_{\mathrm{p}}}\left(\frac{\partial f}{\partial p}\dot{p} + \frac{\partial f}{\partial q}\dot{q}\right) \tag{18}$$

$$K_{\mathrm{p}} = -\left(\frac{\partial f}{\partial \alpha}\bar{\alpha} + \frac{\partial f}{\partial p_0}\bar{p}_0\right) \tag{19}$$

with $\bar{p}_0$ and $\bar{\alpha}$ clearly defined in Equations (15) and (16). The partial derivatives of the yield surface with respect to the stress components and the internal variables entering Equations (18) and (19) can be easily found from Equation (6) as

$$\frac{\partial f}{\partial p} = -2\alpha(q - p\alpha) - 2m^2 p + (2+n)m^2 p\left(\frac{p}{p_0}\right)^n \tag{20a}$$

$$\frac{\partial f}{\partial q} = 2(q - \alpha p) \tag{20b}$$

$$\frac{\partial f}{\partial \alpha} = -2p(q - \alpha p) \tag{20c}$$

$$\frac{\partial f}{\partial p_0} = \frac{-n}{p_0}m^2 p^2\left(\frac{p}{p_0}\right)^n \tag{20d}$$

At this point it must be pointed out that softening, which was described earlier in terms of $\alpha^b - \alpha < 0$ and $\dot{\alpha} < 0$, is related to a negative value of the plastic modulus K_{p} as it should. Indeed, for variable stress-ratio loading where $r_{\mathrm{ef}} \simeq m$, the $\bar{p}_0$ term in Equation (15) is very small due to the negative exponential factor with the very large value of V. Consequently, inserting the expression for $\bar{\alpha}$ from Equation (16) and the foregoing expression (20c) for $\partial f/\partial \alpha$ in Equation (19), one obtains for the plastic modulus the expression $K_{\mathrm{p}} \simeq 2hr_{\mathrm{ef}}p^2(\eta - \alpha)(\alpha^b - \alpha)$, which is negative when $\alpha^b - \alpha < 0$ in triaxial compression (and similarly, with proper change of signs, for triaxial extension). It should also be mentioned that such softening is related to stress ratio rather than stress itself. To see this, one can calculate based on the foregoing equations with $1 - (p/p_0)^n \simeq 1$, that $LK_{\mathrm{p}} = 2p^2(\eta - \alpha)\dot{\eta}$, thus, the $K_{\mathrm{p}} < 0$ implies $\dot{\eta} < 0$ since $L > 0$ always, and not that necessarily $\dot{q} < 0$. This is because for variable stress-ratio loading the model becomes almost identical to the previous versions of SANISAND models with the wedge-type yield surface which are stress ratio controlled. This explains why under undrained conditions the model correctly predicts a diminishing deviatoric stress q but an increasing stress ratio η and still is in the range of hardening response with $K_{\mathrm{p}} > 0$. Softening clearly happens under drained conditions where both q and η decrease when $K_{\mathrm{p}} < 0$.

3. THE SANISAND MODEL IN THE MULTIAXIAL SPACE

The generalization of the triaxial formulation to the multiaxial stress space will be done systematically in a way that explains each step taken for each equation considered. Henceforth, all second-order tensors will be denoted by bold face. The stress tensor is denoted by $\boldsymbol{\sigma}$. The hydrostatic or isotropic stress p and the deviatoric or shear stress tensor $\mathbf{s}$ are defined by $p = (\mathrm{tr}\,\boldsymbol{\sigma})/3$

DOI: 10.1002/nag

and $\mathbf{s} = \boldsymbol{\sigma} - p\mathbf{I}$, where tr means the trace, and $\mathbf{I}$ is the identity tensor. The strain tensor is denoted by $\boldsymbol{\varepsilon}$, while the volumetric strain ε_v and deviatoric strain tensor $\mathbf{e}$ are defined by $\varepsilon_v = \operatorname{tr}\boldsymbol{\varepsilon}$ and $\mathbf{e} = \boldsymbol{\varepsilon} - \varepsilon_v(\mathbf{I}/3)$. As usual, the strain tensor is decomposed into elastic and plastic parts according to Equation (2), and this applies to ε_v and $\mathbf{e}$.

The multiaxial generalization of the constitutive relations is based on the following observation. In triaxial setting any deviatoric symmetric tensor $\mathbf{t}$ develops only normal components t_i $(i = 1, 2, 3)$ with $\operatorname{tr}\mathbf{t} = 0$, which means $t_2 = t_3 = (-1/2)t_1$. It is straightforward to show that the following relation holds true:

$$\tfrac{3}{2}\mathbf{t} : \mathbf{t} = (t_1 - t_3)^2 \tag{21}$$

where the symbol: implies the trace of the product of two adjacent tensors, that is $\mathbf{t} : \mathbf{t} = \operatorname{tr}\mathbf{t}^2$. This is a general equation that constitutes the basis of the current systematic multiaxial generalization. For instance, substituting the deviatoric stress tensor $\mathbf{s}$ into Equation (21), one has $(3/2)\mathbf{s} : \mathbf{s} = (s_1 - s_3)^2$, and knowing that $(s_1 - s_3) = (\sigma_1 - \sigma_3) = q$, the following relation between the deviatoric stress tensor $\mathbf{s}$ and its triaxial counterpart q can be observed when triaxial conditions are assumed:

$$\tfrac{3}{2}\mathbf{s} : \mathbf{s} = q^2 \tag{22}$$

Similarly, substituting the deviatoric strain tensor $\mathbf{e}$ into Equation (21), one obtains $(3/2)\mathbf{e} : \mathbf{e} = (e_1 - e_3)^2$, and knowing that $(e_1 - e_3) = (\varepsilon_1 - \varepsilon_3) = (3/2)\varepsilon_q$, the following relation between the deviatoric strain tensor $\mathbf{e}$ and its triaxial counterpart ε_q can be observed:

$$\tfrac{2}{3}\mathbf{e} : \mathbf{e} = \varepsilon_q^2 \tag{23}$$

Notice the difference between the coefficients in Equations (22) and (23) that directly comes from difference of the definitions for q and ε_q.

3.1. Elastic relations

The multiaxial generalization of the hypoelastic relations (3) is straightforward based on Equations (22) and (23) as

$$\dot{\boldsymbol{\varepsilon}}^{\mathrm{e}} = \dot{\mathbf{e}}^{\mathrm{e}} + \frac{\dot{\varepsilon}_v^{\mathrm{e}}}{3}\mathbf{I} = \frac{\dot{\mathbf{s}}}{2G} + \frac{\dot{p}}{3K}\mathbf{I} \tag{24}$$

with $\mathbf{e}^{\mathrm{e}}$ the deviatoric elastic strain tensor and K and G are the same as in Equations (4) and (5).

3.2. Yield, critical, bounding and dilatancy surfaces

The relation between the deviatoric stress tensor $\mathbf{s}$ and its triaxial counterpart q is already shown in Equation (22). Along the lines of this equation one can introduce the deviatoric stress-ratio tensor $\mathbf{r} = \mathbf{s}/p$, the deviatoric back-stress ratio tensor $\boldsymbol{\alpha}$, and the effective deviatoric stress tensor $\mathbf{s} - p\boldsymbol{\alpha}$, as the multiaxial counterparts of the triaxial entities η, α, and $q - p\alpha$, respectively, such that under triaxial conditions:

$$\tfrac{3}{2}\mathbf{r} : \mathbf{r} = \eta^2, \quad \tfrac{3}{2}\boldsymbol{\alpha} : \boldsymbol{\alpha} = \alpha^2, \quad \tfrac{3}{2}(\mathbf{s} - p\boldsymbol{\alpha}) : (\mathbf{s} - p\boldsymbol{\alpha}) = (q - p\alpha)^2 \tag{25}$$

Notice that Equation (25) implies that $\alpha = \alpha_1 - \alpha_3$, with $\alpha_2 = \alpha_3$ and with the observation that under triaxial conditions the tensor $\boldsymbol{\alpha}$ develops only normal components α_i $(i = 1, 2, 3)$.

DOI: 10.1002/nag

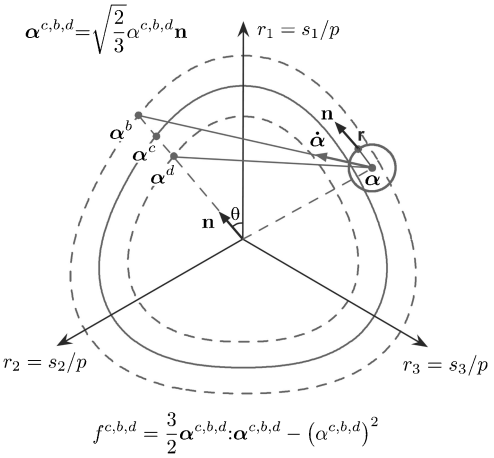

Figure 5. Schematic illustration of model surfaces and mapping definitions of $\boldsymbol{\alpha}^{c,b,d}$ on the stress ratio π-plane.

The generalization of Equation (6) for the yield surface is based on Equation $(25)_3$ and yields

$$f = \tfrac{3}{2}(\mathbf{s} - p\boldsymbol{\alpha}) : (\mathbf{s} - p\boldsymbol{\alpha}) - m^2 p^2 \left[1 - \left(\frac{p}{p_0}\right)^n\right] = 0 \tag{26}$$

Equation (26) represents a very thin closed cone in generalized stress space, which for $p < p_0$ is very similar to the thin open cone generalization of the triaxial wedge-type yield surface in previous versions of SANISAND. The trace of this closed cone with the deviatoric stress ratio π-plane of Figure 5 is shown as a small circle with center at $\boldsymbol{\alpha}$. Unlike the open thin cone which in stress-ratio space had a constant radius proportional to m, here the $\mathbf{r} - \boldsymbol{\alpha}$ varies with p. Besides the singular point at the stress origin where $p = 0$ and $\mathbf{r} = \boldsymbol{\alpha} = 0$, one also has $\mathbf{r} = \boldsymbol{\alpha}$ at tip of the closed cone where $p = p_0$. For $p > p_0$ the closed cone does not intersect the π-plane.

The concept of the other three surfaces of the model, i.e. the critical state, bounding, and dilatancy surfaces, can similarly be generalized to the multiaxial stress space, and it must be emphasized that they are related to the back-stress ratio tensor $\boldsymbol{\alpha}$ rather than the stress-ratio tensor $\mathbf{r}$, for similar reasons presented in the triaxial space in regard to α and η. As already explained in Equations (7) and (8), in the triaxial space the definitions of the critical state, bounding, and dilatancy lines acquire different values of their slopes $\alpha_c^{c,b,d}$ and $-\alpha_e^{c,b,d}$ according to the sign of $\eta - \alpha$, concisely expressed *via* Equation (9). In the multiaxial stress space, the $\alpha^{c,b,d}$ will be interpolated between its compression and extension values, $\alpha_c^{c,b,d}$ and $\alpha_e^{c,b,d}$, by means of the Lode angle θ, according to the proposition by Argyris *et al.* [27], which, with $c = \alpha_e^c/\alpha_c^c$, reads as

$$\alpha^{c,b,d} = g(\theta, c)\alpha_c^{c,b,d} = \frac{2c}{(1+c) - (1-c)\cos 3\theta}\alpha_c^{c,b,d} \tag{27a}$$

$$\cos 3\theta = \sqrt{6}\,\mathrm{tr}\,\mathbf{n}^3, \quad \mathbf{n} = \frac{\mathbf{r} - \boldsymbol{\alpha}}{[(\mathbf{r} - \boldsymbol{\alpha}) : (\mathbf{r} - \boldsymbol{\alpha})]^{1/2}} \tag{27b}$$

DOI: 10.1002/nag

where notice that $\mathrm{tr}\,\mathbf{n}=0$ and $\mathrm{tr}\,\mathbf{n}^2=\mathbf{n}:\mathbf{n}=1$ based on the definition of $\mathbf{n}$. The values $\theta=0$ and $\theta=\pi/3$ correspond to effective stress-ratio definition of compression and extension, respectively, where the effective stress-ratio tensor $\mathbf{r}-\boldsymbol{\alpha}$ (multiaxial counterpart of $\eta-\alpha$) rather than the stress-ratio $\mathbf{r}$ is used to define $\mathbf{n}$ and subsequently θ. Notice that for the extension case now, the $\alpha^{c,b,d}=\alpha_e^{c,b,d}$ and not $-\alpha_e^{c,b,d}$; the later was used with a minus sign for the operation of a direct triaxial formulation. The effect of such difference in sign will be commented in the sequel.

In order to obtain now the exact analytical expression of the critical state, bounding and dilatancy surfaces in the multiaxial space in conjunction with Equations (27a) and (27b), consider a tensor $\boldsymbol{\alpha}^{c,b,d}$ on any one of them. The $\boldsymbol{\alpha}^{c,b,d}$ is the multiaxial generalization of the $\alpha^{c,b,d}$, and since the former is a deviatoric tensor it must satisfy, according to Equation (21), the relation $(3/2)\boldsymbol{\alpha}^{c,b,d}:\boldsymbol{\alpha}^{c,b,d}=(\alpha^{c,b,d})^2$. In fact, this relation can be re-written as

$$f^{c,b,d}=\tfrac{3}{2}\boldsymbol{\alpha}^{c,b,d}:\boldsymbol{\alpha}^{c,b,d}-(\alpha^{c,b,d})^2=0 \tag{28}$$

to represent the analytical expression of the three surfaces, in the stress-ratio π-plane in conjunction with Equations (27a) and (27b). Clearly, Equation (28) are the traces of three open conical surfaces in the π-plane, and their plotting is illustrated in Figure 5. It is good to mention that the above interpolation function results into non-convex curves in the π-plane for some values of c. There are some interpolation rules that do not show the non-convexity, but since no normality is invoked, no problem arises.

An alternative, and more useful, analytical expression for the three surfaces is based on Equation (27a) and can be obtained by the use of polar-type coordinates. Consider a traceless unit tensor $\mathbf{n}$, i.e. $\mathrm{tr}\,\mathbf{n}=0$ and $\mathrm{tr}\,\mathbf{n}^2=1$, emanating from the origin in the π-plane of Figure 5. No relation whatsoever is presently assumed for $\mathbf{n}$ and the one defined in Equation (27b). Equation (28) for the three surfaces can be re-written in the form

$$\boldsymbol{\alpha}^{c,b,d}=\sqrt{\frac{2}{3}}\alpha^{c,b,d}\mathbf{n}=\sqrt{\frac{2}{3}}g\alpha_c^{c,b,d}\mathbf{n} \tag{29}$$

Indeed it is straightforward to verify that the Expression (29) satisfies Equation (28).

The critical state, bounding, and dilatancy 'image' back-stress ratio tensors $\boldsymbol{\alpha}^{c,b,d}$ of $\boldsymbol{\alpha}$ should now be introduced in a way which is consistent with its triaxial counterpart $\alpha^{c,b,d}$. Based on Equation (29), this is very easily accomplished if one identifies the $\mathbf{n}$ that enters Equation (29), with the $\mathbf{n}$ of Equation (27b) that lies along $\mathbf{r}-\boldsymbol{\alpha}$ of the yield surface. The process is illustrated in Figure 5 where the two $\mathbf{n}$'s are purposefully drawn parallel. Clearly, the 'image' back-stress ratio tensors $\boldsymbol{\alpha}^{c,b,d}$ of $\boldsymbol{\alpha}$ are now obtained as the intersections of the directions of $\mathbf{n}$ emanating from the origin, with those surfaces. The analytical expressions for those image stress-ratio tensors are given by Equation (29) in conjunction with Equations (27a) and (27b).

Commenting further on Equation (29), observe that if one sets $\mathbf{t}=\sqrt{2/3}\,t\mathbf{n}$ with $\mathrm{tr}\,\mathbf{n}=0$, $\mathrm{tr}\,\mathbf{n}^2=1$, as the corresponding relation between a triaxial 'stress-like' variable t and its deviatoric multiaxial tensor-valued generalization $\mathbf{t}$ along the lines of Equation (22) (e.g. $\mathbf{t}$ can stand for $\mathbf{s}$, $\mathbf{r}$, $\boldsymbol{\alpha}$, $\boldsymbol{\alpha}^c$, $\boldsymbol{\alpha}^b$, $\boldsymbol{\alpha}^d$, and t can stand for q, η, α, α^c, α^b, α^d, respectively), it can be shown that under triaxial condition where $\mathbf{n}$ is common to all variables, the multiaxial equations become identical to their triaxial counterparts maintaining the *same* model constants, a great advantage for calibration purposes.

DOI: 10.1002/nag

3.3. Flow rule

In the multiaxial space the plastic strain rate $\dot{\boldsymbol{\varepsilon}}^{\mathrm{p}}$ has two components, the deviatoric $\dot{\mathbf{e}}^{\mathrm{p}}$ and volumetric $\dot{\varepsilon}_{\mathrm{v}}^{\mathrm{p}}$. Similar to the triaxial case each one of these two components consists of two contributions that by generalization of Equations (10a), (10b), and (11) are given by

$$\dot{\mathbf{e}}^{\mathrm{p}} = (\dot{\mathbf{e}}^{\mathrm{p}})_1 + (\dot{\mathbf{e}}^{\mathrm{p}})_2 = \langle L \rangle \left[\sqrt{\frac{3}{2}} \mathbf{n} r_{\mathrm{ef}} + \frac{3}{2} X \mathbf{r} \mathrm{e}^{-V r_{\mathrm{ef}}} \right] \tag{30a}$$

$$\dot{\varepsilon}_{\mathrm{v}}^{\mathrm{p}} = (\dot{\varepsilon}_{\mathrm{v}}^{\mathrm{p}})_1 + (\dot{\varepsilon}_{\mathrm{v}}^{\mathrm{p}})_2 = \langle L \rangle [D r_{\mathrm{ef}} + \mathrm{e}^{-V r_{\mathrm{ef}}}] \tag{30b}$$

$$r_{\mathrm{ef}} = \left[\frac{3}{2} (\mathbf{r} - \boldsymbol{\alpha}) : (\mathbf{r} - \boldsymbol{\alpha}) \right]^{1/2} = m \left[1 - \left(\frac{p}{p_0} \right)^n \right]^{1/2} \tag{31}$$

Notice that the r_{ef} becomes $|\eta - \alpha|$ under triaxial conditions (Equation (11)), and the factors $\sqrt{3/2}$ and $3/2$ were introduced in Equations (30a) and (30b) in order to comply with the relation (23) that is the basis for resuming each plastic strain rate contribution of Equation (10a) under triaxial conditions. Recall that at the tip of the closed conical yield surface where $p = p_0$, one has $\mathbf{r} = \boldsymbol{\alpha}$; thus, $\mathbf{n}$ cannot be defined from Equations (27a) and (27b), and $r_{\mathrm{ef}} = 0$. The indefiniteness of $\mathbf{n}$ is not important; however, because with $r_{\mathrm{ef}} = 0$ the first contribution to plastic strain in Equations (30a) and (30b) vanishes, and it is this first contribution that only needs the definition of $\mathbf{n}$ which enters the mechanism associated with the mapping of $\boldsymbol{\alpha}$ onto $\boldsymbol{\alpha}^{c,b,d}$.

With the image $\boldsymbol{\alpha}^d$ of $\boldsymbol{\alpha}$ on the dilatancy surface given by Equation (29) and Equations (27a) and (27b), the generalization of the dilatancy Equation (12) substitutes $(\boldsymbol{\alpha}^d - \boldsymbol{\alpha}) : \mathbf{n}$ for $\alpha^d - \alpha$ of Equation (12) (the need to take the trace of the product with $\mathbf{n}$ appears because D is scalar valued) and one has

$$D = \sqrt{\frac{3}{2}} A_d (\boldsymbol{\alpha}^d - \boldsymbol{\alpha}) : \mathbf{n} = \sqrt{\frac{3}{2}} A_d \left(\sqrt{\frac{2}{3}} \alpha^d \mathbf{n} - \boldsymbol{\alpha} \right) : \mathbf{n} = A_d \left(\alpha^d - \sqrt{\frac{3}{2}} \boldsymbol{\alpha} : \mathbf{n} \right) \tag{32}$$

The factor $\sqrt{3/2}$ was set to multiply A_d, because under triaxial conditions one can set $\boldsymbol{\alpha} = \pm\sqrt{2/3}\, \alpha \mathbf{n}$, in which case Equation (32) for the dilatancy yields $D = A_d(\alpha^d \mp \alpha)$. At first it seems that this expression of D does not match the $D = s A_d(\alpha^d - \alpha)$ of Equation (12) in the direct triaxial formulation; however, recall that the α^d entering Equations (29) and (32) is always positive and becomes either α_c^d or α_e^d, while the α^d in the triaxial formulation was either α_c^d or $-\alpha_e^d$ according to Equation (9). Under these conditions, the two expressions for D are identical, as they should.

3.4. Rate evolution equations for the internal variables

The next step is the rate equations of evolution of the internal variables p_0 and $\boldsymbol{\alpha}$. For the p_0 the same equations as Equation (15) in the triaxial space are assumed, using the equivalent multiaxial expression for r_{ef} as given by Equation (31). The only part that requires generalization is the expression for the dimensionless distance δ in Equation (13) where the scalar α and $g\alpha_c^c$ of the

DOI: 10.1002/nag

triaxial form should be appropriately generalized to the tensors $\boldsymbol{\alpha}$ and $\boldsymbol{\alpha}^c$ based on Equations $(25)_2$ and (29), as

$$\delta = 1 - \frac{p}{p_b}\left[1 + 3\frac{\boldsymbol{\alpha}:\boldsymbol{\alpha}}{(g\alpha_c^c)^2}\right] \tag{33}$$

where notice that $(g\alpha_c^c)^2 = (3/2)\boldsymbol{\alpha}^c:\boldsymbol{\alpha}^c$ according to Equation (28). It must be pointed out that the Lode angle θ entering the definition of g in the above expression is determined from Equation $(27b)_1$ but now the unit tensor $\mathbf{n}_\alpha = \boldsymbol{\alpha}/(\boldsymbol{\alpha}:\boldsymbol{\alpha})^{1/2}$ along $\boldsymbol{\alpha}$ must substitute for $\mathbf{n}$ that was along $\mathbf{r}-\boldsymbol{\alpha}$, since it will be shown that $\mathbf{r}-\boldsymbol{\alpha}=0$ in constant stress ratio loading. For all practical purposes though, one could set $g=1$ in the above equation and avoid the calculation of another Lode angle, with very little effect on the outcome.

Similar to the case for dilatancy, the correct generalization of Equation (16) for $\dot{\alpha}$ to a corresponding equation for $\dot{\boldsymbol{\alpha}}$ uses the bounding 'image' stress-ratio tensor $\boldsymbol{\alpha}^b$ of α on the bounding surface given by Equation (29) in conjunction with Equations (27a) and (27b), and reads

$$\dot{\boldsymbol{\alpha}} = \langle L\rangle h r_{\text{ef}}(\boldsymbol{\alpha}^b - \boldsymbol{\alpha}) = \langle L\rangle \bar{\boldsymbol{\alpha}} \tag{34}$$

where now r_{ef} is defined in Equation (31) and the definition of $\bar{\boldsymbol{\alpha}}$ is self-evident. Observe again the 'attractor' role of $\mathbf{r}$ due to the presence of the 'attractor' term r_{ef} in Equation (34), as in Equation (16) for triaxial. Under constant stress-ratio $\mathbf{r}$ loading, which implies that the point $\mathbf{r}$ in Figure 5 is fixed, the motion of $\boldsymbol{\alpha}$ toward $\boldsymbol{\alpha}^b$ portrayed by Equation (34), and the definition of $\boldsymbol{\alpha}^b$ according to Equation (29), will result into a changing $\boldsymbol{\alpha}^b$ in such a way that eventually $\boldsymbol{\alpha}$ will be moving on the radius connecting the origin with the fixed $\mathbf{r}$, toward an $\boldsymbol{\alpha}^b$ that is also on this radius. But the presence of r_{ef} in the equation for $\dot{\boldsymbol{\alpha}}$ will prevent $\boldsymbol{\alpha}$ from reaching $\boldsymbol{\alpha}^b$ and, instead, will force it to converge with $\mathbf{r}$ that lies on its path toward $\boldsymbol{\alpha}^b$. When this happens, $r_{\text{ef}}=0$ and $\dot{\boldsymbol{\alpha}}=0$, indicating that no further rotation occurs. Again $r_{\text{ef}}=0$ means $\mathbf{r}-\boldsymbol{\alpha}=0$; thus, the $\mathbf{n}$ cannot be defined without consequences, though, since the first contribution does not operate anyway in this case. Further comments on this type of kinematic hardening with 'attractor' can be found in [25].

The multiaxial form of the reference diameter b_{ref} of the bounding surface in Equation (17a) follows the general rule of Equation (22) and is of the form $\mathbf{b}_{\text{ref}} = \sqrt{2/3}\, b_{\text{ref}}\mathbf{n}$ with $b_{\text{ref}} = \alpha_c^b + \alpha_e^b$. The generalized form of h in Equation (17a) reads as

$$h = \frac{b_0}{(\frac{3}{2})((\mathbf{b}_{\text{ref}} - (\boldsymbol{\alpha}^b - \boldsymbol{\alpha})):\mathbf{n})^2} \tag{35}$$

which acquires its triaxial form once it is specialized to the triaxial setting. To see this, consider the triaxial case where one has $\mathbf{b}_{\text{ref}} = \sqrt{2/3}\, b_{\text{ref}}\mathbf{n}$, $\boldsymbol{\alpha}^b = \sqrt{2/3}\, \alpha^b\mathbf{n}$, and $\boldsymbol{\alpha} = \pm\sqrt{2/3}\, \alpha\mathbf{n}$. Then the denominator of Equation (35) becomes $(b_{\text{ref}} - \alpha^b \pm \alpha)^2$. Again at first it may seem different from the denominator $(b_{\text{ref}} - s(\alpha^b - \alpha))^2$ of Equation (17b), but recalling again that α^b in Equation (35) is always a positive α_c^b or α_e^b, while the α^b in Equation (17b) was defined as either α_c^b or $-\alpha_e^b$, the two denominator expressions are identical. Equation (17b) can still be used for finding b_0 without any change.

DOI: 10.1002/nag

3.5. Loading index and plastic modulus

The completion of the model requires satisfaction of the consistency condition $\dot{f}=0$ applied to Equation (26), which in conjunction with Equations (15) and (16) yields

$$L=\frac{1}{K_{\mathrm{p}}}\left(\frac{\partial f}{\partial \boldsymbol{\sigma}}:\dot{\boldsymbol{\sigma}}\right)=\frac{1}{K_{\mathrm{p}}}\left(\frac{\partial f}{\partial \mathbf{s}}:\dot{\mathbf{s}}+\frac{\partial f}{\partial p}:\dot{p}\right) \tag{36}$$

$$K_{\mathrm{p}}=-\left(\frac{\partial f}{\partial \boldsymbol{\alpha}}:\bar{\boldsymbol{\alpha}}+\frac{\partial f}{\partial p_0}\bar{p}_0\right) \tag{37}$$

with $\bar{p}_0$ and $\bar{\boldsymbol{\alpha}}$ clearly defined in Equations (15) and (16). The partial derivatives of the yield surface with respect to the stress and the internal variables can be easily found from Equation (6) as

$$\frac{\partial f}{\partial \boldsymbol{\sigma}}=\frac{\partial f}{\partial \mathbf{s}}+\frac{1}{3}\frac{\partial f}{\partial p}\mathbf{I} \tag{38a}$$

$$\frac{\partial f}{\partial p}=-3\boldsymbol{\alpha}:(\mathbf{s}-p\boldsymbol{\alpha})-2m^2p+(2+n)m^2p\left(\frac{p}{p_0}\right)^n \tag{38b}$$

$$\frac{\partial f}{\partial \mathbf{s}}=3(\mathbf{s}-p\boldsymbol{\alpha}) \tag{38c}$$

$$\frac{\partial f}{\partial \boldsymbol{\alpha}}=-3p(\mathbf{s}-p\boldsymbol{\alpha}) \tag{38d}$$

$$\frac{\partial f}{\partial p_0}=\frac{-n}{p_0}m^2p^2\left(\frac{p}{p_0}\right)^n \tag{38e}$$

It is important to indicate now how softening can be described in the multiaxial setting. Similar to the triaxial formulation, for variable stress-ratio loading for which $r_{\mathrm{ef}}\simeq m$, the $\bar{p}_0$ term in Equation (15), which applies to multiaxial as well, is very small due to the negative exponential factor with the very large value of V. Consequently, inserting the expression for $\bar{\boldsymbol{\alpha}}$ from Equation (34) and the foregoing expression (38d) for $\partial f/\partial\boldsymbol{\alpha}$ in Equation (37), one obtains for the plastic modulus the expression $K_{\mathrm{p}}\simeq 3hr_{\mathrm{ef}}p^2(\mathbf{r}-\boldsymbol{\alpha}):(\boldsymbol{\alpha}^b-\boldsymbol{\alpha})$. Given the variation of $\boldsymbol{\alpha}^b$ with ψ, it is possible to have $\boldsymbol{\alpha}$ placed outside the bounding surface in such a way that the 'inner' product $(\mathbf{r}-\boldsymbol{\alpha}):(\boldsymbol{\alpha}^b-\boldsymbol{\alpha})<0$, thus, $K_{\mathrm{p}}<0$, which signifies softening in terms of the stress ratio $\mathbf{r}$. To see this, based on the foregoing equations with $1-(p/p_0)^n\simeq 1$ and recalling the relation $\mathbf{s}=p\mathbf{r}$, one can find after some algebra from Equation (36) that $LK_{\mathrm{p}}=3p^2(\mathbf{r}-\boldsymbol{\alpha}):\dot{\mathbf{r}}$. Thus, since $L>0$ always, the $K_{\mathrm{p}}<0$ implies $(\mathbf{r}-\boldsymbol{\alpha}):\dot{\mathbf{r}}<0$, which can be interpreted geometrically in stress ratio space as the motion of $\mathbf{r}$ in a direction 'opposite' to $\mathbf{r}-\boldsymbol{\alpha}$, i.e. 'inwards' from the current position of the yield surface that is basically what happens in softening. Reference to Figure 5 can illustrate the foregoing, although the setting is not addressing exactly the case of softening as described above.

DOI: 10.1002/nag

Table I. Triaxial and multiaxial formulations of the SANISAND model.

Triaxial formulation	Multiaxial formulation
Elasticity	
$\dot{\varepsilon}_q^{\mathrm{e}} = \dot{q}/(3G)$	$\dot{\mathbf{e}}^{\mathrm{e}} = \dot{\mathbf{s}}/(2G)$
$\dot{\varepsilon}_{\mathrm{v}}^{\mathrm{e}} = \dot{p}/K$	$\dot{\varepsilon}_{\mathrm{v}}^{\mathrm{e}} = \dot{p}/K$
Yield surface	
$f = (q - p\alpha)^2$	$f = (3/2)(\mathbf{s} - p\boldsymbol{\alpha}) : (\mathbf{s} - p\boldsymbol{\alpha})$
$\quad -m^2 p^2[1 - (p/p_0)^n] = 0$	$\quad -m^2 p^2[1 - (p/p_0)^n] = 0$
Flow rule	
$\dot{\varepsilon}_q^{\mathrm{p}} = \langle L \rangle [s r_{\mathrm{ef}} + X\eta \mathrm{e}^{-V r_{\mathrm{ef}}}]$	$\dot{\mathbf{e}}^{\mathrm{p}} = \langle L \rangle [\sqrt{3/2}\mathbf{n} r_{\mathrm{ef}} + (3/2) X \mathbf{r} \mathrm{e}^{-V r_{\mathrm{ef}}}]$
$\dot{\varepsilon}_{\mathrm{v}}^{\mathrm{p}} = \langle L \rangle [D r_{\mathrm{ef}} + \mathrm{e}^{-V r_{\mathrm{ef}}}]$	$\dot{\varepsilon}_{\mathrm{v}}^{\mathrm{p}} = \langle L \rangle [D r_{\mathrm{ef}} + \mathrm{e}^{-V r_{\mathrm{ef}}}]$
$r_{\mathrm{ef}} = \lvert \eta - \alpha \rvert$	$r_{\mathrm{ef}} = [(3/2)(\mathbf{r} - \boldsymbol{\alpha}) : (\mathbf{r} - \boldsymbol{\alpha})]^{1/2}$
Evolution laws	
$\dot{\alpha} = \langle L \rangle h(\alpha^b - \alpha) r_{\mathrm{ef}}$	$\dot{\boldsymbol{\alpha}} = \langle L \rangle h(\boldsymbol{\alpha}^b - \boldsymbol{\alpha}) r_{\mathrm{ef}}$
$\dot{p}_0 = \langle L \rangle p_0 (1 + e) \mathrm{e}^{-V r_{\mathrm{ef}}} /$	
$\quad [e(\rho_c - (p_0/p_{\mathrm{at}})^{1/3}/K_0)(1 - (\operatorname{sgn} \delta)\lvert\delta\rvert^{\theta})]$	
$h = b_0/[b_{\mathrm{ref}} - s(\alpha^b - \alpha)]^2$	$h = b_0/[(3/2)(\mathbf{b}_{\mathrm{ref}} - (\boldsymbol{\alpha}^b - \boldsymbol{\alpha})) : \mathbf{n}]^2$
$D = s A_d (\alpha^d - \alpha)$	$D = \sqrt{3/2} A_d (\boldsymbol{\alpha}^d - \boldsymbol{\alpha}) : \mathbf{n}$
$s = (q - p\alpha)/\lvert q - p\alpha \rvert$	$\mathbf{n} = (\mathbf{s} - p\boldsymbol{\alpha})/\lvert \mathbf{s} - p\boldsymbol{\alpha} \rvert$
$\alpha^{c,b,d} = s g \alpha_c^{c,b,d}$	$\boldsymbol{\alpha}^{c,b,d} = \sqrt{2/3} g \alpha_c^{c,b,d} \mathbf{n}$
$\alpha_c^b = \alpha_c^c \exp(-n^b \psi)$	
$\alpha_c^d = \alpha_c^c \exp(n^d \psi)$	
Yield surface derivatives	
$\partial f/\partial p = -2\alpha(q - p\alpha) - 2m^2 p$	$\partial f/\partial p = -3\boldsymbol{\alpha} : (\mathbf{s} - p\boldsymbol{\alpha}) - 2m^2 p$
$\quad + (2 + n) m^2 p (p/p_0)^n$	$\quad + (2 + n) m^2 p (p/p_0)^n$
$\partial f/\partial q = 2(q - \alpha p)$	$\partial f/\partial \mathbf{s} = 3(\mathbf{s} - p\boldsymbol{\alpha})$
$\partial f/\partial \alpha = -2p(q - \alpha p)$	$\partial f/\partial \boldsymbol{\alpha} = -3p(\mathbf{s} - p\boldsymbol{\alpha})$
$\partial f/\partial p_0 = -(n/p_0) m^2 p^2 (p/p_0)^n$	$\partial f/\partial p_0 = -(n/p_0) m^2 p^2 (p/p_0)^n$

Such softening mechanism with the back-stress ratio $\boldsymbol{\alpha}$ placed outside the bounding surface was first described in the first version of SANISAND model by Manzari and Dafalias [1].

Having the values $\partial f/\partial p$, $\partial f/\partial \mathbf{s}$, $\partial f/\partial \boldsymbol{\alpha}$ and $\partial f/\partial p_0$, it is now straightforward to observe that when one specializes the multiaxial formulation to triaxial, Equations (36) and (37) provide the same loading index L and plastic modulus K_{p} as the triaxial Equations (18) and (19). Table I presents the major triaxial and multiaxial constitutive equations of SANISAND model in the first and second columns, respectively, in direct correspondence with each other, while the expressions which are common to both are listed under the first column only. The general

DOI: 10.1002/nag

logic employed in generalizing the model equations from triaxial to multiaxial space can be clearly observed in this table. Observe also that by setting $1-(p/p_0)^n=1$ and simply omitting any reference to the derivatives and hardening in regard to p_0, as well as noting that the term $\exp(-Vr_{\text{ef}})\simeq 0$, one obtains all the equations of the previous versions of SANISAND models employing the open wedge- or cone-type yield surfaces, with small modifications in details such as the new form of h, the $3/2$ factor instead of the $1/2$ in Equation (26) for the yield surface, etc.

4. CALIBRATION OF MODEL CONSTANTS

The proposed model requires calibration of 16 parameters, two sets of which are shown for two sands in Table II divided in different groups according to the particular role they play. The material parameters can be selected mainly from standard types of laboratory tests. The first part of calibration requires drained and/or undrained triaxial compression and extension tests at different values of initial void ratio and confining pressure in order to calibrate different features of hardening/softening and dilatancy/contractancy of the model that are associated with the first plastic strain rate contribution due to stress-ratio changes, exactly as it was done in previous SANISAND model versions. The other part of calibration is related to the LCC, which is incorporated for capturing the elasto-plastic response under constant stress-ratio loading. Isotropic (or one-dimensional) compression data for specimens loaded to high-confining pressures is needed for this part. Pestana and Whittle [13, 14] have proposed the related parameters based on published data for more than 20 different sands. Finally, in order to capture the shear response under constant stress-ratio test with non-zero η, essentially generalizing the Pestana and Whittle proposition from $\eta=0$ to $\eta\neq 0$, one needs data of such kind of test (or data of K_0 loading test), if available, which can be used to find the parameter X.

Table II. Parameters of the SANISAND model for Toyoura sand and Sacramento river sand.

Parameter		Toyoura sand	Sacramento river sand
Elasticity	G_0 (kPa)	125	200
	K_0 (kPa)	150	130
CSL	α_c^c	1.2	1.3
	c	0.712	0.65*
	e_0	0.934	0.96
	λ	0.019	0.028
	ξ	0.7	0.7
Dilatancy	n^d	2.1	2.0
	A_d	0.4	0.8
Kinematic hardening	n^b	1.25	1.3
	h_0	36.96	22.75
	c_h	0.987	1.03
LCC	p_r (kPa)	5500	3150
	ρ_c	0.37	0.37
	θ	0.18	0.22
	X	0.8*	0.8*

*Assumed.

DOI: 10.1002/nag

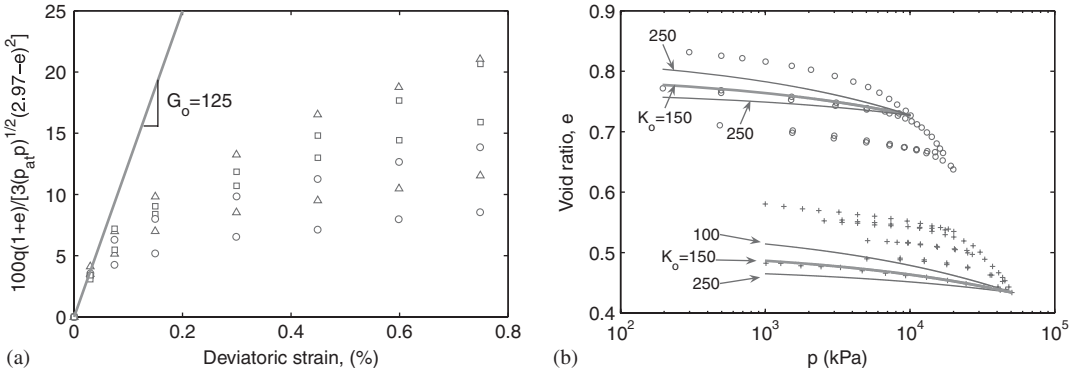

Figure 6. Calibration of G_0 and K_0 constants using data of drained triaxial compression and hydrostatic unloading tests on isotropic consolidated Toyoura sand. Data after Verdugo and Ishihara [28], Miura [29], and Miura *et al.* [30].

The general procedure of calibrating the constants of the model addressing the variable stress-ratio loading, as well as simulations for evaluating the corresponding performance of the model, has been presented in previous works, e.g. [2, 3]. For the sake of completeness and in order to show the performance of the current version of SANISAND, the calibration process of the model and simulation of some available laboratory experiments are repeated. Details of the calibration will be presented in the following section with reference to Toyoura sand database from Verdugo and Ishihara [28], Miura [29], and Miura *et al.* [30].

4.1. Elasticity parameters

The G_0 parameter that defines the elastic shear modulus of sand in Equation (5) can be calibrated using the stress–strain curves or from the elastic wave propagation tests in the field or laboratory. In this paper, a good estimation of G_0 for monotonic shearing in Toyoura sand is obtained by fitting Equation (4) to the initial stages of the deviatoric stress–strain ($\varepsilon_q - q$) data of triaxial drained tests. Hence, according to Figure 6(a) a value of $G_0 = 125$ kPa is selected for Toyoura sand.

The K_0 parameter that controls the elastic bulk modulus of sand in Equation (4) can be obtained from data of unloading in isotropic compression tests, assuming isotropic behavior at load reversal. Miura [29] and Miura *et al.* [30] have conducted a set of isotropic compression and swelling tests on Toyoura sand, which can be used for calibration of K_0. Figure 6(b) shows that $K_0 = 150$ kPa gives reasonable results for almost all of the swelling paths in this set of data.

4.2. Critical state line parameters

The critical state parameters consist of $\alpha_{c,e}^c$ the critical back-stress ratio in triaxial compression and extension (or α_c^c and $c = \alpha_e^c/\alpha_c^c$), and the parameters $(e_c)_{\text{ref}}$, λ_c, and ξ of Equation (1) that define the position of the CSL in the void ratio-mean effective stress. Calibration of these parameters requires monotonic tests that approach critical state.

The values of α_c^c and c can be simply calibrated by plotting the results of the triaxial tests at the critical state in the p–q space. Similarly the parameters e_0, λ_c, and ξ can be obtained by fitting

DOI: 10.1002/nag

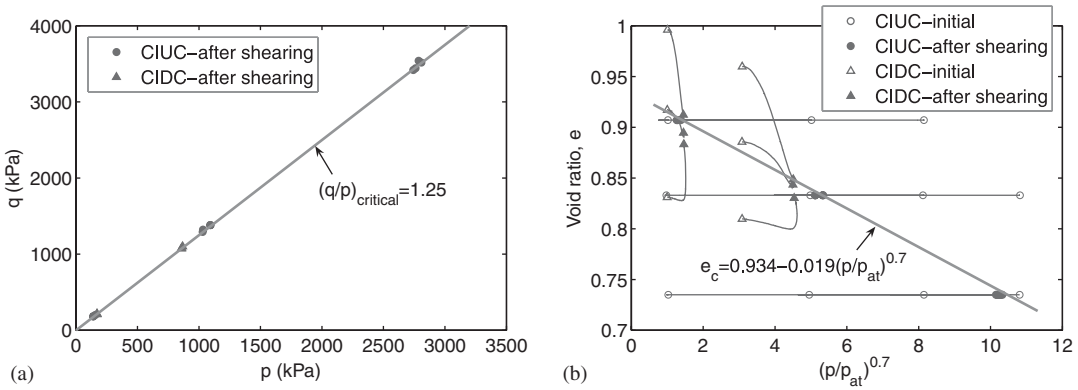

Figure 7. Calibration of CSL constants for Toyoura sand using the results of CIDC and CIUC tests. Data after Verdugo and Ishihara [28].

the best curve to the results of triaxial test at critical state in the $e - p/p_{\text{at}}$ space. Results of the drained and undrained triaxial compression tests on Toyoura sand are presented in Figure 7. It can be observed from Figure 7(a) that $M = (q/p)_{\text{critical}} = 1.25$ gives a good approximation of the critical stress ratio for triaxial compression, and, therefore, α_c^c can be approximately chosen as $\alpha_c^c = M - m = 1.25 - 0.05 = 1.2$. Similar procedure can be followed for the triaxial extension test; however, here the value of $c \simeq 0.75$ is adopted from [4]. Figure 7(b) offers a distinct CSL with the following linear relation between e_c and $(p/p_{\text{at}})^{0.7}$, which is consistent with the suggested equation by Li and Wang [17]:

$$e_c = 0.934 - 0.019(p/p_{\text{at}})^{0.7} \tag{39}$$

4.3. Dilatancy parameters

The parameter n^d can be determined by evaluating Equation (8) at the phase transformation state, at which $D = 0$. It follows from Equations (8), (9), and (12) that

$$n^d = \frac{1}{\psi^d} \ln\left(\frac{\alpha^d}{\alpha^c}\right) \tag{40}$$

where ψ^d and α^d are the values of ψ and α (or η) at the phase transformation state, measured from drained or undrained test results. Recall that α^c can be either α_c^c or $-\alpha_e^c$ for triaxial compression or extension; the sign of α^d must also be negative in Equation (40) if applied to extension. Note that the phase transformation state corresponds to the peak of the volumetric strain ε_{v} in drained tests and the peak of the excess pore pressure $u - u_0$ in undrained tests. A good estimate of the value of n^d can be obtained by plotting the α^d/α^c *versus* the respective ψ^d of different tests. It is obvious that the interpolation should pass through $\alpha^d/\alpha^c = 1$ for $\psi = 0$ that refers to the critical state. For instance, the plot of α^d/α^c *versus* ψ^d for Toyoura sand from different drained and undrained tests is shown in Figure 8(a) leading to $n^d \simeq 2.1$. Notice that this value differs from $n^d = 3.5$ used in Dafalias and Manzari [3] and such difference can be simply

DOI: 10.1002/nag

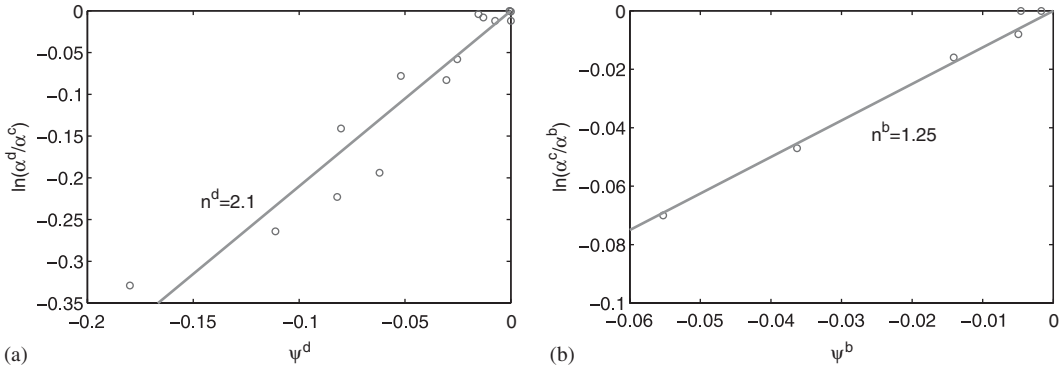

Figure 8. Calibration of constants n^d and n^b for Toyoura sand using the results of CIDC and CIUC tests. Data after Verdugo and Ishihara [28].

attributed to the more precise interpretation of the experimental data achieved by the plot in Figure 8(a).

The direct estimation of the dilatancy parameter A_d requires good quality stress–dilatancy data. In a drained test, ignoring the small elastic deformations one has

$$\frac{\dot{\varepsilon}_{\mathrm{v}}}{\dot{\varepsilon}_q} \simeq \frac{\dot{\varepsilon}_{\mathrm{v}}^{\mathrm{p}}}{\dot{\varepsilon}_q^{\mathrm{p}}} = A_d(\alpha^d - \alpha) \tag{41}$$

The parameter A_d can then be calibrated based on $\varepsilon_{\mathrm{v}} - \varepsilon_q$ curves.

4.4. Kinematic hardening parameters

In a similar approach to evaluation of n^d, the parameter n^b can be determined by evaluating Equations (7) and (9) at the peak stress ratio, where $b = 0$. Hence,

$$n^b = \frac{1}{\psi^b} \ln\left(\frac{\alpha^c}{\alpha^b}\right) \tag{42}$$

where ψ^b and α^b are the values of ψ and α (or η) at the peak stress-ratio state, measured from drained or undrained test results. Again recall from Equations (7) and (9) that α^c is α_c^c for compression and $-\alpha_e^c$ for extension, while also the α^b should be assigned a negative value for extension. Processed results from drained triaxial tests on Toyoura sand are presented in Figure 8(b), where $n^b \simeq 1.25$ can be selected for this sand.

The remaining parameters related to the effect of distance from bounding surface in Equation (17b) are h_0 and c_h which are generally estimated by trial and error.

4.5. Compression parameters

The model requires the isotropic compression data for specimens loaded to high-confining pressures corresponding to the LCC regime for calibration of the p_r, ρ_c, and θ parameters. These pressures are typically in the range of $p = 10$–50 MPa for siliceous sands [13] but could be smaller for

DOI: 10.1002/nag

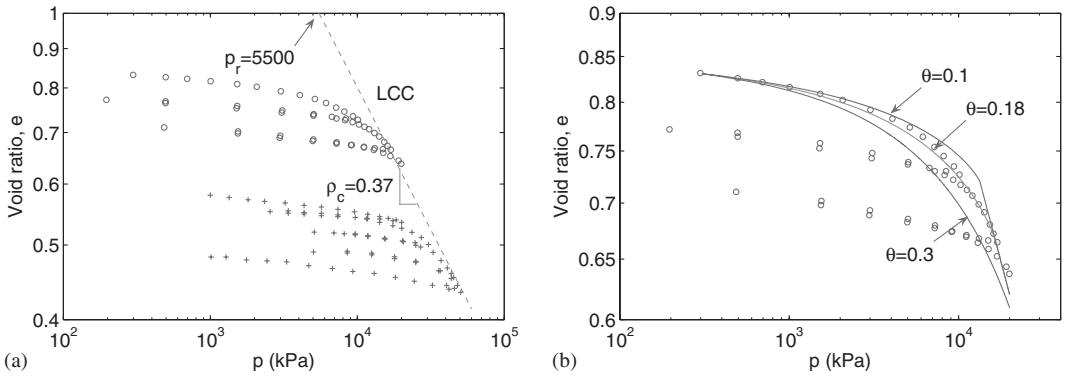

Figure 9. Calibration of LCC parameters using data of isotropic compression test on Toyoura sand. Data after Miura [29] and Miura *et al.* [30].

gypsum and Calcareous Sands. Pestana and Whittle [13] have shown how these three parameters can be readily estimated from hydrostatic compression tests, and they have also reported selected values for these parameters for a wide range of cohesionless soils. The p_r and ρ_c are the reference stress (at $e = 1.0$) and slope of the linearized LCC in $\log e - \log p$ space and θ characterizes the elasto-plastic transition. The position of the LCC for Toyoura sand is shown in Figure 9, which offers $p_r = 5500\,\text{kPa}$ and $\rho_c = 0.37$. Parameter θ controls the transitional regime from low stresses to stresses in the LCC regime and has been found to depend on angularity and material gradation [31]. Figure 9 illustrates the determination of parameter θ for Toyoura sand where $\theta = 0.18$ gives acceptable results for the elasto-plastic transition regime. More details of the effects of mineralogy, particle angularity, D_{50}, and particle size distribution on the values of these parameters can be found in Pestana and Whittle [13, 14].

Unfortunately, the authors could not find experimental results for constant stress-ratio loading with non-zero η on Toyoura sand in the literature for proper calibration of the corresponding parameter X. However, as already presented in Figure 10, McDowell *et al.* [24] have reported results of constant stress-ratio tests for both $\eta = 0$ (isotropic compression) and $\eta = 1$ loading on *Silica sand*. These sets of data can be used for calibration of X. In order to do so, the corresponding compression parameters were re-calibrated for this new sand so as to properly capture the volumetric response. For the case of $\eta = 0$, the values $K_0 = 120\,\text{kPa}$, $p_r = 4200\,\text{kPa}$, $\rho_c = 0.5$, and $\theta = 0.3$ were obtained as explained before for the Toyoura sand. For the case of $\eta = 1$, the same parameters were used. Results of the simulation are presented in Figure 10(a) in terms of variations of void ratio, e, and mean effective pressure, p, for both $\eta = 0$ and 1. In a task to calibrate the X parameter, the authors concluded that the choice of $X \simeq 0.8$ is appropriate in order to capture the deviatoric strains as presented in Figure 10(b). This can be used as the default value for X. It is important to observe that the definition of the δ given in Equation (13) that accounts for the effect of the non-zero stress ratio results into the convergence with differently located LCC lines for $\eta = 0$ and 1 using the same set of model constants. In fact, this is an appropriate point to illustrate the effect of the eventuality to have a negative value of the distance δ defined in Equation (13) for triaxial and Equation (33) for multiaxial space. This effect was discussed after Equation (14) and can be visualized as follows. Consider first an isotropic

DOI: 10.1002/nag

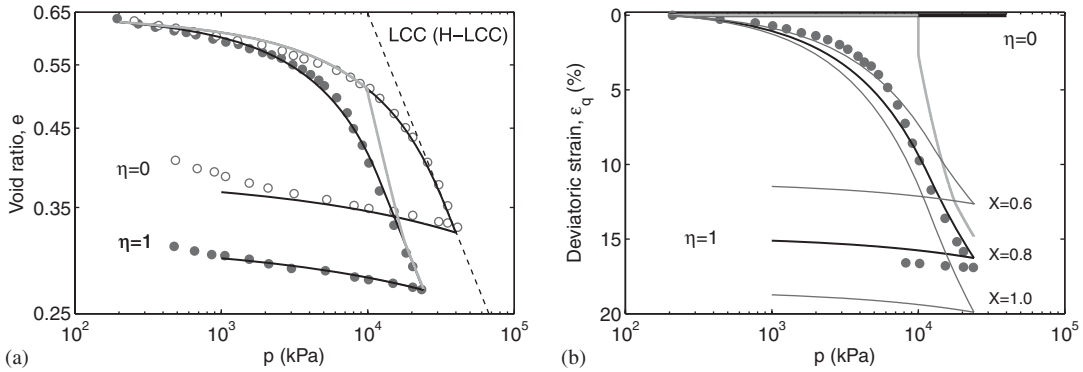

Figure 10. Comparison of data and simulations for constant stress ratio loading with $\eta = 0$ and 1 on Silica sand. Data after McDowell *et al.* [24]. The gray line illustrates the response when changing η value from 0 to 1 during consolidation and the effect of the resulting negative value of δ as discussed after Equation (14).

consolidation at $\eta = 0$ till $p = 10^4$ kPa; then an increase of q till $\eta = q/p = 1$, followed by further increase of p at constant $\eta = 1$ till $p = 2.4 \times 10^4$ kPa. In Figure 10(a) the response of the model in the e–p space is shown by the gray continuous curve. During isotropic consolidation, the curve follows exactly the previous simulation for $\eta = 0$ as expected, while the change to $\eta = 1$ loading is characterized by a progressive transition of the curve from the simulation at $\eta = 0$ to convergence with the simulation at $\eta = 1$. Such transition/convergence response is due to negative value the distanced δ acquired because of the sudden change of the stress ratio η from 0 to 1, as explained after Equation (14). The deviatoric response shows a corresponding transition as shown in Figure 10(b).

Table II presents the calibrated parameters for Toyoura and Sacramento river sands. These parameters have been used for the simulations that are presented in the next section. One should also know that the default values $m = 0.05$, $n = 20$, and $V = 1000$ in Equations (6) and (10a) are used. Such default values do not need calculation for most cases of interest.

5. MODEL PERFORMANCE

The model has been implemented numerically using the procedure outlined by Bardet and Choucair [32]. This procedure linearizes the constraints of laboratory loadings, links them to the constitutive relations, and forms a linear system of ordinary differential equations. Using this approach one can simply simulate any stress-control, strain-control, or stress–strain-control test. For solving the system of ordinary differential equations, the simplest integration technique—the forward Euler method—is employed and thus small loading steps (stress or strain increments) are to be used to insure convergence and good accuracy.

This section presents performance of the SANISAND model under various loading paths and drainage conditions. More specifically it compares data and simulations for drained and undrained triaxial monotonic tests as well as drained isotropic compression and swelling tests. In all, this section compares data and simulations from 33 laboratory tests performed by

DOI: 10.1002/nag

Verdugo and Ishihara [28], Miura [29], Miura *et al.* [30], and Lee and Seed [33] on Toyoura sand and Sacramento river sand.

5.1. Toyoura sand

Toyoura sand is uniform fine quartzitic sand consisting of sub-rounded to sub-angular particles, which is the standard cohesionless soil reported in the Japanese soil mechanics literature [28–30, 34–36]. Verdugo and Ishihara [28] have conducted a complete set of monotonic drained and undrained triaxial tests on isotropically consolidated samples of Toyoura sand with a mean diameter $D_{50} = 0.17$ mm and a uniformity coefficient $C_u = 1.7$. These tests have been conducted on a wide range of void ratios and confining pressures and have been used for evaluation of the previous versions of SANISAND [2, 3]. In order to assess the performance of the most recent version of the model, this set of data has been again used in this paper.

Figure 11 compares the data and simulations for undrained triaxial compression (CIUC) tests on isotropically consolidated samples of Toyoura sand. In particular, Figure 11(a) makes the comparison in terms of effective stress paths, while Figure 11(b) does the same in terms of stress–strain response for the dense samples ($e_{\text{in}} = 0.735$) with initial confining pressures in the range of 100 to 3000 kPa. Similar comparison between data and simulations at medium dense ($e_{\text{in}} = 0.833$) and loose ($e_{\text{in}} = 0.907$) samples are presented in Figure 11(c)–(f), respectively. It should be pointed out in accord with the observations for softening made after Equations (20), that the strong reduction of the deviatoric stress q observed for some of the looser samples with higher initial confining pressure p does not imply softening in terms of the stress ratio η that keeps increasing till critical failure. Figure 12 compares the data and the simulations for drained triaxial compression (CIDC) tests on isotropically consolidated samples of Toyoura sand. In particular, Figure 12(a) makes the comparison in terms of variations of void ratio with shear stress, while Figure 12(b) does the same in terms of variations of axial strain with shear stress for the loose, medium and dense samples of Toyoura sand with initial confining pressure of 100 kPa. Similarly Figure 12(c) and (d) compares the data and simulations of CIDC tests with initial confining pressure of 500 kPa. It should also be pointed out that now the slight reduction of q observed for the denser samples is also followed by a corresponding reduction of the stress ratio η because of the drained loading conditions, which is a true stress-ratio softening in accord with the comments made after Equations (20).

The dramatically different responses that result from different combinations of confining pressure p and void ratio e can be all successfully captured by using a unique set of model constants. The response varied from highly dilatant in higher densities and lower confining pressures to highly contractant in lower densities and higher confining pressures. The key to this achievement lies with the variation of α_c^b and α_c^d with ψ, here portrayed by Equations (7) and (8). Very good match has been achieved in the undrained simulations; however, one can observe a comparative shortcoming of the model in accurately capturing the drained response. To be more specific, the simulations have underpredicted the volumetric strains in the drained tests. This could be solved by choosing larger values of dilatancy parameter A_d; however, this will affect the perfect match in the undrained simulations. Dafalias and Manzari [3] had chosen the larger A_d value to get better matches in the drained simulations, while they had used an unrealistic small value of Poisson's ratio to still get good match in the undrained test. That choice of unrealistic small Poisson's ratio overpredicts the elastic volumetric response, which does not agree with the observations in the swelling parts of the isotropic compression tests in Figure 6(b). In the current paper it was

DOI: 10.1002/nag

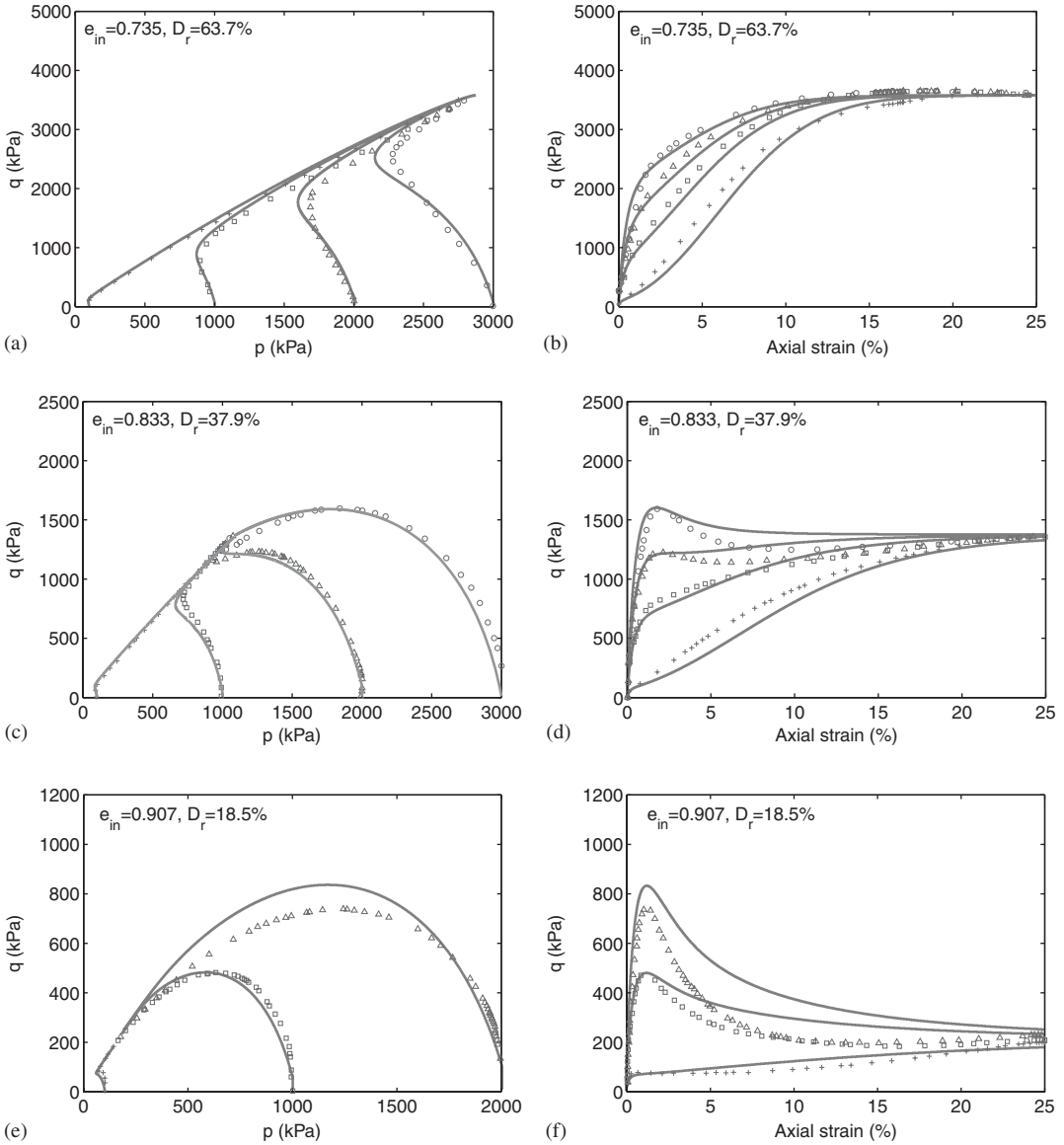

Figure 11. Comparison of data and simulations for undrained triaxial compression tests on isotropically consolidated samples of Toyoura sand ($e_{\text{in}} = 0.735$, 0.833, and 0.907). Data after Verdugo and Ishihara [28].

preferred to use the realistic elastic bulk modulus paying the price of some deviations in the drained simulations.

Figure 13 compares data and simulations for isotropic compression tests with cycles of unloading (swelling) and reloading up to high values of confining pressure on initially loose and dense samples

DOI: 10.1002/nag

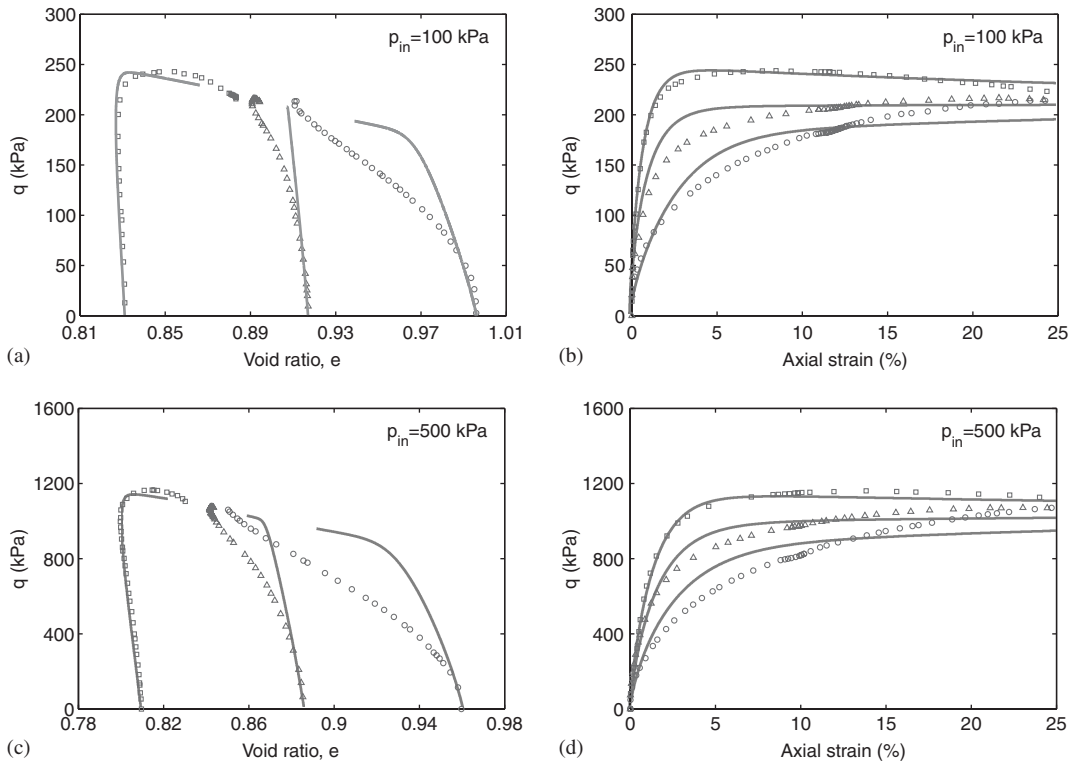

Figure 12. Comparison of data and simulations for drained triaxial compression tests on isotropically consolidated samples of Toyoura sand ($p_{\text{in}} = 100$ and 500 kPa). Data after Verdugo and Ishihara [28].

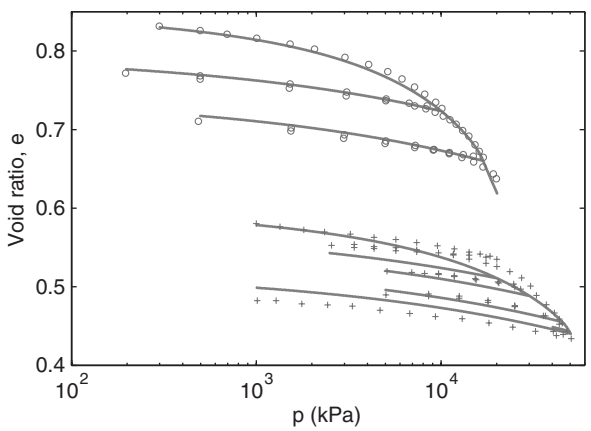

Figure 13. Comparison of data and simulations for isotropic compression tests on initially loose and dense samples of Toyoura sand ($e_{\text{in}} = 0.83$ and 0.58). Data after Miura [29] and Miura *et al.* [30].

DOI: 10.1002/nag

of Toyoura sand. The simulations show the full capability of the integrated LCC concept [13] in the model. although the large plastic response is evident in the high pressures, it can also be observed in the moderate pressure for the very loose samples.

5.2. *Sacramento river sand*

Lee and Seed [33] conducted a series of drained triaxial compression (CIUC) tests on isotropically consolidated samples of Sacramento river sand on a wide range of initial densities and confining pressures. These results have been used by numerous researchers in the past for validating their constitutive models [19, 32, 37, 38]. Figure 14 shows the comparison of data and simulations for undrained triaxial compression (CIUC) tests on isotropically consolidated samples of loose and dense Sacramento river sand. In particular, Figure 14(a) makes the comparison in terms of variations of volumetric–axial strains, while Figure 14(b) does the same in terms of stress–strain response for the loose samples ($e_{\text{in}} \simeq 0.86$) with initial confining pressures in the range of 100–1240 kPa. Similarly comparison between data and simulations for dense ($e_{\text{in}} = 0.60$) samples are presented in Figure 14(c) and (d). The loose sample under high initial cell pressure undergoes considerable compaction, while under low initial cell pressure it shows a mild dilation despite being in a loose state. In case of the dense samples, depending on the initial cell pressure the samples show different degrees of dilation. The softening and hardening responses can be observed from the ε_a–q plots.

It is good to note that the results of CIDC tests by Lee and Seed [33] do not really show a unique CSL for the loose and dense samples of Sacramento river sand as pointed out by Bardet [37]. To find the CSL with any accuracy, one should make sure that the sample is contractive to begin with. Physically the dense samples show localized deformation and shear bands in larger strains; hence, the void ratio of the sample will not be uniformly distributed anymore. In particular, the average void ratio of the specimen for a dense sample is almost always less than the void ratio in the bands of shearing soil, which really is at critical state. This means that one may observe different locations for the CSL in the e–p space if he relies on global measurements, but the real CSL is the one attained by the loose samples. In this paper the CSL probe identified by the loose Sacramento river sand is considered as the average CSL and the dense sample simulations are done up to only 10% of the axial strains where the non-uniformities are milder. Still the minor discrepancies in Figure 14(c) can be attributed to the above-mentioned fact. There could also be other reasons for the non-uniqueness of the CSL as a result of possible differences in the sample preparation methods, an issue that has been the subject of some recent debate, but the authors keep working on the assumption of unique CSL in this work.

Lee and Seed [33] have also reported results of isotropic compression tests with unloading and reloading on loose and dense samples of Sacramento river sand. These results are perfect to show the new feature of the model in simulation of constant stress-ratio loading. Figure 15(a) shows the comparison of data and simulations for the isotropic compression tests samples of Sacramento river sand at different initial void ratios ranging from 0.61 to 0.87, while Figure 15(b) does the same thing for cycles of loading and unloading during isotropic compression tests on initially loose and dense samples. The importance of the elasto-plastic simulations feature of the model, especially for the looser samples, can be observed form these plots. Very good agreement can be observed between the simulations and experimental results, which confirms the good capability of the LCC concept and its adaptation in this work.

DOI: 10.1002/nag

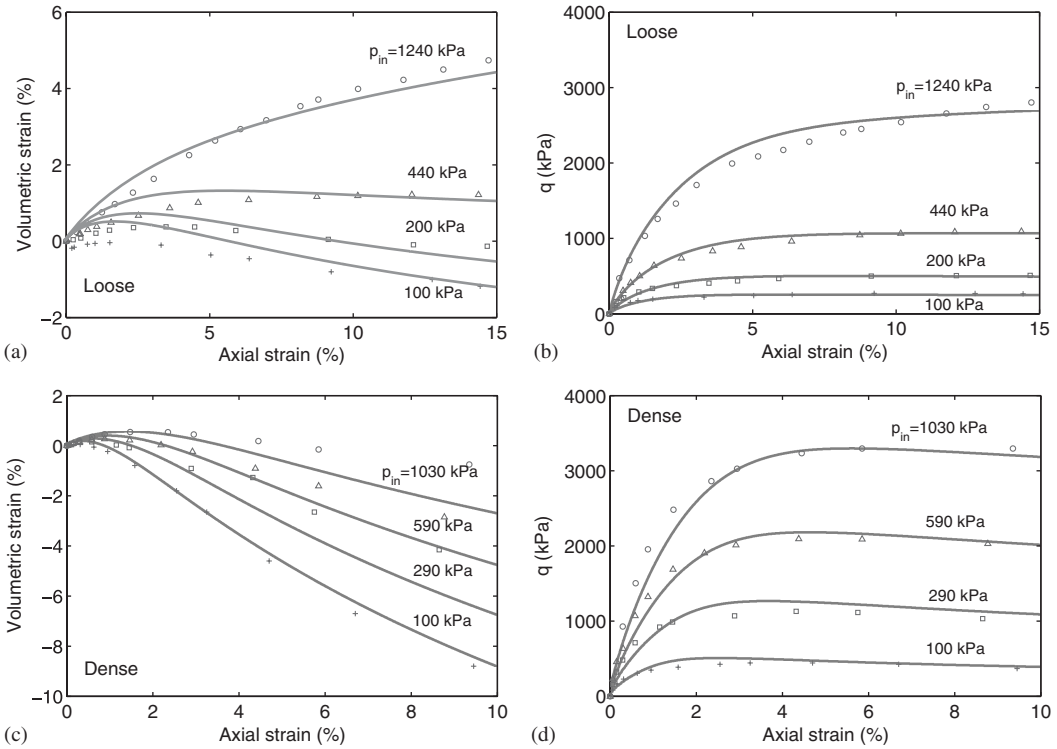

Figure 14. Comparison of data and simulations for drained triaxial compression tests on isotropically consolidated loose and dense samples of Sacramento river sand. Data after Lee and Seed [33].

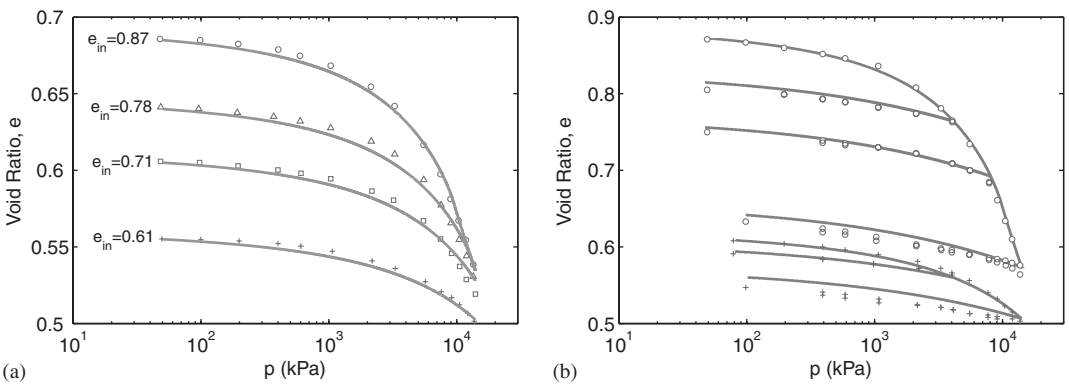

Figure 15. Comparison of data and simulations for isotropic compression tests on Sacramento river sand. Data after Lee and Seed [33].

DOI: 10.1002/nag

6. SUMMARY AND CONCLUSION

The paper presents the constitutive equations, the calibration procedure, and the simulative capabilities of a new member of the SANISAND family of models. In this version of the model the inability of previous versions to induce plastic deformation under constant stress-ratio loading is eliminated. The keys to this elimination are two: First, the introduction of a single closed and narrow yield surface that is very similar to the previously used narrow open wedge in triaxial or narrow open cone in multiaxial space. Second, it is the use of a pre-investigated mechanism by Pestana and Whittle [13] for reproducing plastic strains up to high values of confining pressure. The idea for generalizing this mechanism to any constant stress-ratio loading is also adopted from Pestana and Whittle [14] and is presented in conjunction with a corresponding isotropic hardening mechanism. The new features are added in a way that the model has retained all of its previously well-established features. Another improvement is the elimination of the need for initial values of (back) stress ratio, a discrete memory parameter that was needed in the earlier version of the model. This is a very good improvement for implicit coding of the model. All of the constitutive equations are presented in both the triaxial and the multiaxial stress space for better understanding of the underlying concepts, such understanding enhanced by the systematic way the transition from triaxial to multiaxial is reasoned. The SANISAND model is shown to provide successful simulation of both drained and undrained behavior of sands in triaxial and isotropic compression tests in a large range of confining pressures. The required features for capturing the constant stress-ratio compression loading with non-zero stress-ratio values are foreseen in the model, but the authors could not find related data for the examined sands to investigate the quantitative response in these situations. The cyclic response of the model, which as expected is quite similar to what is shown in its earlier version due to the narrowness of the new yield surface, is planned to be discussed in a later publication.

The anisotropy in the present version, as in the original first member of the SANISAND models family [1], is due to the rotational/kinematic hardening feature. In the present version, the rotational hardening has been considerably altered from the one in the previous versions, because the closed type yield surface necessitates the convergence of the rotational variable with the stress ratio when constant stress-ratio loading takes place. This alteration is based on the use of an attractor term in the evolution equation of the rotational variable, along the lines of the corresponding concept in SANICLAY [25]. Finally, it is worth mentioning that a new concept of hardening transition was introduced by activating and deactivating in a smooth way, employing an exponential transition factor (the one associated with the constant V), different hardening mechanisms depending on the location of the stress point on the yield surface. This was done in conjunction with the introduction of two distinct contributions to the plastic strain-rate depending on the constant or variable stress-ratio character of loading. Such new constitutive concepts can be used in other plasticity models as well, not necessarily only for soils.

Additional constitutive ingredients addressing issues of inherent and evolving fabric anisotropy [3, 4] are simple add-ons features that can be incorporated in the present version as done in the forgoing references.

ACKNOWLEDGEMENTS

The supports from the NSF grant No. CMS-02-01231 of the program directed by Dr Richard Fargazy, and the Office of Graduate Studies at the University of California at Davis are gratefully acknowledged.

DOI: 10.1002/nag

Professor X. S. Li and Professor J. P. Bardet kindly provided digitized data of the experimental results on Toyoura sand and Sacramento River sand to the authors.

REFERENCES

1. Manzari MT, Dafalias YF. A critical state two-surface plasticity model for sands. *Géotechnique* 1997; **47**(2): 255–272.
2. Li XS, Dafalias YF. Dilatancy for cohesionless soils. *Géotechnique* 2000; **54**(4):449–460.
3. Dafalias YF, Manzari MT. Simple plasticity sand model accounting for fabric change effects. *Journal of Engineering Mechanics* 2004; **130**(6):622–634.
4. Dafalias YF, Papadimitriou AG, Li XS. Sand plasticity model accounting for inherent fabric anisotropy. *Journal of Engineering Mechanics* 2004; **130**(11):1319–1333.
5. Vermeer PA. Double hardening model for sand. *Géotechnique* 1978; **28**(4):413–433.
6. Sture S, Runesson K, Macari EJP. Analysis and integration of a three-invariant plasticity model for granular materials. *Archive of Applied Mechanics* (*Ingenieur-Archiv*) 1989; **59**:253–266.
7. Yang BL, Dafalias YF, Herrmann LR. Bounding surface plasticity model for concrete. *Journal of Engineering Mechanics* 1985; **111**(3):359–380.
8. Wang ZL, Dafalias YF, Shen CK. Bounding surface hypoplasticity model for sand. *Journal of Engineering Mechanics* 1990; **116**(5):983–1001.
9. Lourenço PB, de Borst R, Rots JG. A plane stress softening plasticity model for orthotropic materials. *International Journal for Numerical and Analytical Methods in Geomechanics* 1997; **40**(21):4033–4057.
10. Simo JC, Kennedy JG, Govindjee S. Non-smooth multisurface plasticity and viscoplasticity. Loading/unloading conditions and numerical algorithms. *International Journal for Numerical Methods in Engineering* 1988; **26**: 2161–2185.
11. Pramono E, Willam K. Implicit integration of composite yield surfaces with corners. *Engineering Computations* 1989; **6**:186–197.
12. Collins IF. The concept of stored plastic work or frozen elastic energy in soil mechanics. *Géotechnique* 2005; **55**(5):373–382.
13. Pestana JM, Whittle AJ. Compression model for cohesionless soils. *Géotechnique* 1995; **45**(4):611–631.
14. Pestana JM, Whittle AJ. Formulation of a unified constitutive model for clays and sands. *International Journal for Numerical and Analytical Methods in Geomechanics* 1999; **23**(12):1215–1243.
15. Schofield AN, Wroth CP. *Critical State Soil Mechanics*. McGraw-Hill: London, 1968.
16. Wood DM. *Soil Behaviour and Critical State Soil Mechanics*. Cambridge University Press: Cambridge, 1990.
17. Li XS, Wang Y. Linear representation of steady-state line for sand. *Journal of Geotechnical and Geoenvironmental Engineering* 1998; **124**(12):1215–1217.
18. Been K, Jefferies MG. A state parameter for sands. *Géotechnique* 1985; **35**(2):99–112.
19. Crouch RS, Wolf JP, Dafalias YF. Unified critical state bounding surface plasticity model for soil. *Journal of Engineering Mechanics* (ASCE) 1994; **120**(11):2251–2270.
20. Russell AR, Khalili N. Drained cavity expansion in sands exhibiting particle crushing. *International Journal for Numerical and Analytical Methods in Geomechanics* 1999; **26**(4):323–340.
21. Richart FE, Hall JR, Woods RD. *Vibration of Soils and Foundations*, *International Series in Theoretical and Applied Mechanics*. Prentice-Hall: Englewood Cliffs, NJ, 1970.
22. Lawrence JD. *A Catalog of Special Plane Curves*. Dover: New York, 1972.
23. Papadimitriou AG, Bouckovalas GD, Dafalias YF. Plasticity model for sand under small and large cyclic strains. *Journal of Geotechnical and Geoenvironmental Engineering* 2001; **127**(11):973–983.
24. McDowell GR, Nakata Y, Hyodo M. On the plastic hardening of sand. *Géotechnique* 2000; **52**(5):349–358.
25. Dafalias YF, Manzari MT, Papadimitriou AG. Saniclay: simple anisotropic clay plasticity model. *International Journal for Numerical and Analytical Methods in Geomechanics* 2006; **30**(12):1231–1257.
26. Dafalias YF. Bounding surface plasticity. I: Mathematical foundations and hypoplasticity. *Journal of Engineering Mechanics* (ASCE) 1986; **112**(9):966–987.
27. Argyris JH, Faust G, Szimmat J, Warnke EP, Willam KJ. Recent developments in the finite element analysis of prestressed concrete reactor vessels. *Nuclear Engineering and Design* 1974; **282**(1):42–75.
28. Verdugo R, Ishihara K. The steady state of sandy soils. *Soils and Foundations* 1996; **36**(2):81–91.
29. Miura N. A consideration on the stress–strain relation of a sand under high pressures. *Proceedings of the Japan Society of Civil Engineers* 1979; **282**(2):127–130.

DOI: 10.1002/nag

30. Miura N, Murata H, Yasufuku N. Stress–strain characteristics of sand in a particle-crushing region. *Soils and Foundations* 1984; **24**(1):77–89.
31. Pestana JM, Whittle AJ, Salvati LA. Evaluation of a constitutive model for clays and sands; Part I: sand behaviour. *International Journal for Numerical and Analytical Methods in Geomechanics* 1999; **26**(11):1097–1121.
32. Bardet JP, Choucair W. A linearized integration technique for incremental constitutive equations. *International Journal for Numerical and Analytical Methods in Geomechanics* 1991; **15**(1):1–19.
33. Lee KL, Seed HB. Drained strength characteristics of sands. *Journal of the Soil Mechanics and Foundations Division* 1967; **93**(SM6):117–141. Proceedings of the American Society of Civil Engineers.
34. Miura N, Yamanouchi T. Effect of water on the behavior of a quartz-rich sand under high stress. *Soils and Foundations* 1975; **15**(4):23–34.
35. Ishihara K. Liquefaction and flow failure during earthquakes. *Géotechnique* 1993; **43**(3):351–415.
36. Yoshimine M, Ishihara K, Vargas W. Effects of principal stress direction and intermediate principal stress on drained shear behavior of sand. *Soils and Foundations* 1998; **38**(3):177–186.
37. Bardet JP. Bounding surface plasticity model for sands. *Journal of Engineering Mechanics* 1986; **112**(11): 1198–1217.
38. Wang ZL, Dafalias YF, Li XS, Makdisi FI. State pressure index for modeling sand behavior. *Journal of Geotechnical and Geoenvironmental Engineering* 2002; **128**(6):511–519.

DOI: 10.1002/nag